Single-cell plasticity in mouse visual cortex following retinal lesions

Rosa M. García-Verdugo

München 2015

Single-cell plasticity in mouse visual cortex following retinal lesions

Dissertation

zur Erlangung des Grades

eines Doktors der Naturwissenschaften

der Fakultät für Biologie

der Ludwig-Maximilians-Universität München

vorgelegt von

Rosa María García-Verdugo

20. April 2015

Erstgutachter:	Professor Dr. Mark Hübener
Zweitgutachter:	Professor Dr. Hans Straka
Promotionsgesuch eingereicht am:	20. April 2015
Datum der mündlichen Prüfung:	3. Juli 2015

Eidesstattliche Erklärung:

Ich versichere hiermit an Eides statt, dass ich die Dissertation mit dem Titel “Single-cell plasticity in mouse visual cortex following retinal lesions“ selbstständig und ohne unerlaubte Beihilfe angefertigt habe. Ich habe mich dabei keiner anderen als der von mir ausdrücklich bezeichneten Hilfen und Quellen bedient.

Erklärung:

Hiermit erkläre ich, dass ich mich nicht anderweitig einer Doktorprüfung ohne Erfolg unterzogen habe. Die Dissertation wurde in ihrer jetzigen oder ähnlichen Form bei keiner anderen Hochschule eingereicht und hat noch keinen sonstigen Prüfungszwecken unterzogen.

München, 20. April 2015

Rosa María García-Verdugo

Lo bueno, si breve, dos veces bueno

(Baltasar Gracián, 1601-1658)

Contents

List of Figures

Summary

Plasticity is a key feature of virtually all brains. It is thought to underlie learning and memory, and it plays a crucial role during the early development of neural circuits. But plasticity is by no means restricted to developmental periods. In the mammalian visual cortex, as well as in other primary sensory areas, this capacity is maintained in adulthood. A long established model to induce adult plasticity in the visual cortex is based on partial retinal lesions. In this thesis, I have made use of a mouse retinal lesion model to investigate, at the single-cell level and in a chronic manner, adult plasticity with a particular focus on changes of receptive field architecture.

Earlier work in higher mammals has shown that following retinal lesions cells located within the lesion projection zone (LPZ) initially lose their responsiveness and then shift their receptive fields to neighboring positions in the visual field outside the deprived area. This process is known as “filling-in”, and in mice leads to an almost full recovery of activity within the LPZ. During this process, receptive field size also increases. Taking advantage of the combination of two-photon microscopy and a genetically-encoded calcium indicator, I sought to investigate these changes at the level of individual neurons over time. I mapped the receptive fields of neurons in the primary visual cortex (V1) of mice before and over two months after small retinal lesions, determined the shift and direction of the newly formed receptive fields and measured the change in receptive field size over this period. I compared two distinct regions for analysis: regions close (100µm-200µm away)

and far (more than 350µm away) from the LPZ. The results show that receptive fields from neurons located close to the LPZ suffer a significantly larger shift from their baseline position than do those located far from it. On average, for receptive fields close to the LPZ, the direction of the shift pointed away from the LPZ. Receptive field sizes increased in both regions in the early phase of the recovery, although to a larger extent for cells close to the LPZ. Over the course of recovery, receptive field sizes declined again, with cells far from the LPZ reverting back to baseline.

I further analyzed visually-driven activity levels for the two aforementioned regions before and after sensory deprivation. I found a significant reduction of visually-evoked activity in regions close to the LPZ, whereas there was hardly any change in those far from it. In accordance with this finding, after estimating the mean peak amplitude at the preferred orientation for cells located in either of the two regions, I uncovered a significant decrease in peak amplitude for neurons close to the LPZ that was maintained for at least a month after the retinal lesion. In contrast, changes in peak amplitude for cells located far from the LPZ were not significantly different from baseline.

A key property of neurons in V1 is orientation selectivity. Previous studies on functional plasticity after retinal lesions have paid only limited little attention to this property and, moreover, came to somewhat contradicting results. To determine the effects of small retinal lesions on orientation tuning in mice, I assessed orientation selectivity, the preferred orientation and direction and bandwidth before and after sensory deprivation. I found that overall neurons close to the LPZ show slightly less stable orientation selectivity, with more cells losing, gaining or changing their orientation selectivity after retinal lesions than those far from it. When I compared the shift from preferred orientation, preferred direction and bandwidth after retinal lesions for cells close and far from the LPZ, I found no significant differences in any of these parameters. Taken together, these results suggest that changes to orientation tuning after retinal lesions are marginal in mice, similar to what has been observed in monkeys.

In this study, I have been able, for the first time, to chronically map receptive field properties of large populations of neurons. I demonstrate that plastic changes to receptive fields reported after retinal lesions in monkeys and cats also hold true for mice. Finally, orientation tuning is barely affected by this form of sensory deprivation.

Abbreviations

AAV Adeno-associated virus

ACSF Artificial cerebrospinal fluid

ANOVA Analysis of variance

BW Band width

CCD Charge-coupled device

close Region close to the LPZ

cpd Cycles per degree

cps Cycles per second

DI Direction index

DMSO Dimethyl sulfoxide

far Region far from LPZ

GABA γ-aminobutyric acid

HEPES 4-(2-hydroxyethyl)-1-piperazineethanesulfonic acid

HLS Hue, lightness, saturation

Abbreviations

LGN Lateral geniculate nucleus

LFP Local field potential

LPZ Lesion projection zone

MD Monocular deprivation

OGB1-AM Oregon Green Bapta-1,AM

OI Optical imaging of intrinsic signals

OSI Orientation selectivity index

PrefDir Preferred direction

PFA Paraformaldehyde

PrefOri Preferred orientation

SC Superior collicullus

RL Retinal lesion

RF Receptive field

SD Standard deviation

SEM Standard error of the mean

SNR Signal to noise ratio

V1 Primary visual cortex

1

Introduction

1.1 Mouse primary visual cortex.

Mice have been widely used for studies on vision, in particular during the last decade (Bayer [6]), mainly due to their amenability to genetic manipulation and their small brain size, which allows the study of neuronal populations over entire brain regions (Wang and Burkhalter [81]). This advantage has been further extended recently with the development of new light based imaging technologies, such as two-photon microscopy (Helmchen and Denk [33]), which allow monitoring many neurons at the same time, even chronically, taking advantage of genetically-encoded calcium indicators (Grienberger and Konnerth [32], Chen et al. [14]). Another reason why mice have become a model for research on the mammalian visual system is that mouse V1 (primary visual cortex) neurons display similar response properties as have been described for higher mammals including spatial frequency tuning, orientation tuning, receptive fields, contrast gain control and contrast invariant orientation (Niell and Stryker [62]).

While a relatively new model for studies on vision, the main stages of visual processing in mice are well known. In short, light is detected by photoreceptors located in the retina and transduced into neuronal signals, which, through a number of intermediate cells, arrive at retinal ganglion cells (RGC), of which a majority project to the lateral geniculate nucleus (LGN) in the thalamus, first step of visual information processing in the brain. Of

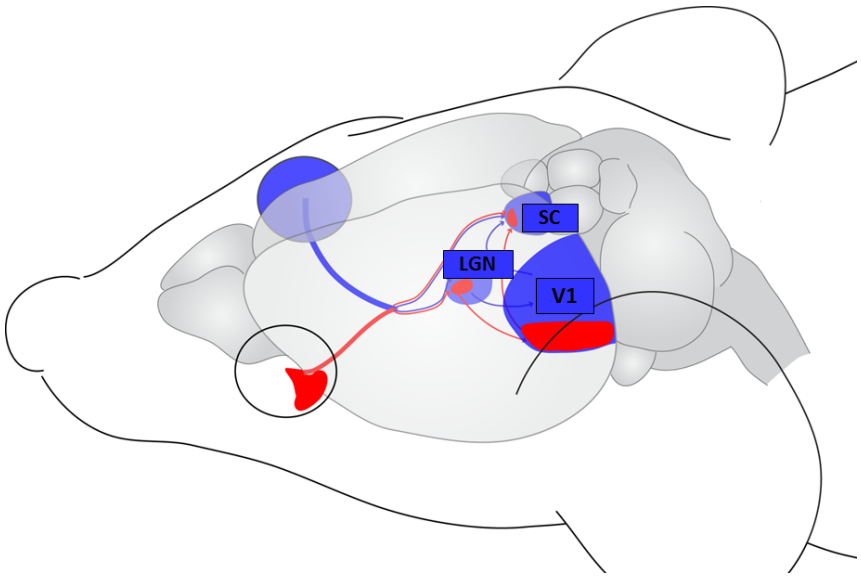

Figure 1.1.1 – Mouse visual system (from Wilks et al. [82]). dLGN: dorsal lateral geniculate nucleus. SC: superior collicullus. V1: primary visual cortex. Red: ipsi. Blue: contra. Ganglion cells in the nasal part of the retina (blue), and processing the peripheral field of view, project their axons across the midline at the optic chiasm to the contralateral hemisphere, while axons from a small number of temporal ganglion cells (red), processing visual input from the central field of view, remain ipsilateral. Retinal ganglion cell axons, which form the optic nerve, terminate in the lateral geniculate nucleus (LGN), where ipsilateral (red) and contralateral (blue) inputs stay segregated. From the LGN, neurons project to the primary visual cortex (V1), which is subdivided into a monocular (blue) and a binocular (red) region. Binocular V1 receives input from both eyes, while monocular V1 processes input from the contralateral eye only. Creative Commons licence.

all RGC axons projecting to the LGN, only a minority (~2%) remain on the ipsilateral side, while most cross over to the contralateral hemisphere at the optic chiasm (Dräger and Olsen [22]). Thalamocortical axons conveying information from the contralateral eye only converge into the monocular region of V1 whereas axons processing visual input both from the ipsilateral and contralateral eye do it in the most lateral third of V1 and constitute the binocular cortex (Métin et al. [61], Dräger [21]).

In mice, V1 in the same way as the rest of the cerebral cortex, is organized in six layers which overall show the inter-laminar connectivity pattern described for other mammals. The majority of fibers projecting from the LGN into V1 innervate cells in layer 4 (Valverde [80]) which in turn synapse onto layer 2/3 cells (Gilbert and Wiesel [28]), these connect in turn to layer 5 cells via their apical tufts (Gilbert and Wiesel [29]). Layer 5 neurons connect to layer 6 cells, which synapse back onto layer 4 cells. In layer 2/3 most projections are

cortico-cortical, whereas layer 5 constitutes the main output layer with connections to subcortical structures (Douglas and Martin [20]) such as the superior colliculus (Hübener and Bolz [44]), the lateral posterior nucleus of the thalamus (Lund et al. [56]) and the pons (Albus and Donate-Oliver [2]). Layer 6 sends feed-back projections to the LGN (Gilbert and Kelly [27], Gilbert and Wiesel [28]).

Although the anatomical organization and basic functional properties are shared with most mammals used in vision studies (cats, ferrets, monkeys), there are a number of characteristics that are specific to mouse V1. Mice, despite showing a "typical" retinotopic map, as has been, for example demonstrated by optical imaging of intrinsic signals (Schuett et al. [70]) lack this organization at the microscopic level, as demonstrated by Smith and Häusser [72], who also showed that receptive fields are relatively scattered in visual space within local subpopulations, a fact corroborated by Bonin et al. [10]. Moreover, receptive fields (RFs) are far larger in mice (10°-12 °) than in cats (~1°) or monkeys (<1°) (Hübener [42]).

Another important difference is that cortical columns, which are based on functional properties, and are typical of carnivores and most primates (Hubel and Wiesel [40], Hubel et al. [41]) are missing in mice. "Pin-wheel" orientation maps (Bonhoeffer and Grinvald [9]) are not found in mice. Rather, cells with different orientation preferences are arranged in what is termed a "salt-and-pepper" organization (Dräger and Olsen [22], Ohki et al. [63]).

Despite these differences, orientation tuning in mice is very similar to that in cats or monkeys (Niell and Stryker [62]). A large proportion of V1 cells is orientation selective, and a substantial proportion of these cells are also direction selective (Mangini and Pearlman [58], Métin et al. [61]), and respond differentially to the direction of motion of a visual stimulus.

Orientation selective neurons can differ in the phase-dependence of their response to moving gratings. Simple cells are classically defined as having an elongated receptive field with separate on and off subfields placed side by side. Complex cells, in contrast,

typically have a homogeneous receptive field without discrete on/off subfields and show therefore, a phase-invariant response to moving gratings (Hubel and Wiesel [40]).

Recent studies have investigated the circuitry underlying orientation tuning. Excitatory and inhibitory neurons in V1 have been found to differ in their orientation tuning in mice, the latter being much more broadly tuned (Niell and Stryker [62], Kerlin et al. [49]). In agreement with this fact inhibitory neurons receive strong synaptic input from a diverse population of selective excitatory neurons (Runyan et al. [69]). Excitatory neurons, on the other hand, establish connections preferably with other neurons sharing the same orientation preference (Hofer et al. [35], Ko et al. [52, 51], Cossell et al. [15]), although their excitatory synaptic input is quite broad and strongest at the preferred orientation (Liu et al. [55]). Similarly, the inhibitory synaptic input to excitatory neurons is broadly tuned, even more so than the excitatory (Niell and Stryker [62], Kerlin et al. [49]) and also strongest at their preferred orientation. It is this interplay between excitatory and inhibitory input which has been shown to explain the sharpening of orientation tuning (Liu et al. [55]).

1.2 Adult plasticity

A neural mechanism hypothesized to underlie learning and memory is synaptic plasticity. In response to specific patterns of external input, neurons can strengthen or weaken their synaptic connections by the addition of new synapses or removal of the existing ones. Synaptic plasticity is heightened during development, and especially during so-called critical periods, where the capacity for plasticity in certain sensory modalities is greatly enhanced, after which it declines over time in an age dependent manner. However, there are brain regions such as the hippocampus, the striatum or the cerebellum, where synaptic plasticity is maintained even during adulthood (Hübener and Bonhoeffer [43]).

But adult plasticity is not restricted to the aforementioned brain regions, also the neocortex has been demonstrated to show adult plasticity even in primary sensory areas like somatosensory (Merzenich et al. [60]), auditory (Robertson and Irvine [68], Recanzone et al. [66]) and visual cortex (Gilbert et al. [26], Kaas et al. [45], Gilbert [25], Keck et al. [47, 48], Calford et al. [13]). The wealth of knowledge derived from studies of critical period plasticity in the latter system made it an important model for studies of adult plasticity, since the resulting structural and functional changes became easier to interpret in light of prior knowledge.

1.2.1 Adult plasticity in visual cortex

Adult plasticity was first shown in the mammalian visual cortex by Kaas and colleagues (Kaas et al. [45]), and later by Gilbert and colleagues (Gilbert et al. [26], Gilbert [25], Gilbert and Wiesel [30]). Kaas and colleagues performed matching retinal lesions ranging in size from 5° to 10° in visual field to both eyes in cats and found that cortical neurons that would have normally had their receptive fields (RF) in this lesioned part of the retina had shifted their receptive field positions to retinal regions surrounding the lesion site. Later, Gilbert and Wiesel (Gilbert and Wiesel [30]) found that, in both monkeys and cats, binocular matching retinal lesions alter receptive fields of cortical cells in a staged fashion. First, immediately after the lesion, the recording sites with receptive fields close to the center of the deprived cortical region originally innervated by the lesioned part of the retina (lesion projection zone, LPZ) became unresponsive. However, at sites where the RFs where at the boundary of the LPZ, they underwent a large increase in receptive field size as well as a small centrifugal shift in their position from the center of the lesion. Two months after the lesion, receptive field sizes were much smaller than those found right after the lesion. However, a much larger shift in receptive field position, of even up to 5°, was detected in recording sites with RFs originally located at the center of the lesioned retina. The extent and direction of receptive field shifts after binocular retinal lesions can be observed in figure 1.2.1. This work also proved that, after retinal lesions, there is no

functional recovery at the level of the lateral geniculate nucleus (LGN). That, together with anatomical studies that show that the spread of geniculocortical afferents is insufficient to provide a basis for the observed cortical recovery (Darian-Smith and Gilbert [17], Das and Gilbert [18]), pointed to horizontal cortico-cortical connections as being responsible for the recovery. This hypothesis was later supported by Palagina et al. [65]: Using voltage-sensitive dye recordings in rats after retinal lesions, they could demonstrate that shortly after the lesion the majority of cells inside the LPZ became activated by the propagation of activity derived from unaffected cortical regions. At later time points, the latencies of the responses of these cells inside the LPZ decreased and the activation reached supra threshold levels. The horizontal propagation of the excitation wave from outer regions into the LPZ and the subsequent facilitation of synaptic activity corroborate the important role of cortical horizontal connections in the functional reorganization achieved after retinal lesions.

Summarizing these results briefly, the functional recovery after retinal lesions follows this pattern: immediately after the lesion, and for up to 2-4 weeks thereafter, cells in the LPZ become silent. Consequently, in a process known as 'filling-in" (Gilbert [25], Gilbert and Wiesel [30]), a few neurons inside the LPZ with visual field locations corresponding to the border of the retinal lesion regain activity. Soon thereafter, more cells inside this region start acquiring new receptive fields just outside of it. As a result of this process the cortical map of retinotopic preference becomes distorted (Hübener and Bonhoeffer

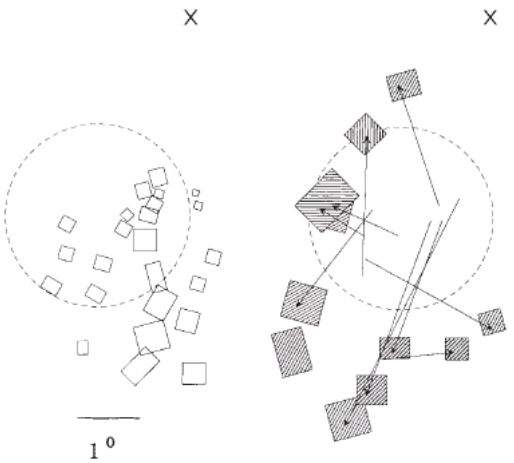

Figure 1.2.1 – Receptive fields shift to position outside the LPZ two months after retinal lesions in monkeys; from Gilbert and Wiesel [30]. Left: receptive field positions before the lesion. Right: two months after binocular retinal lesions. X marks foveal position. Dashed line: LPZ border. Reprint permission: 3667651214933.

[43]).

More detailed studies on the nature of the functional and structural changes caused by retinal lesions have been undertaken in recent years. For instance, Giannikopoulos and Eysel [24] found, by performing single-cell recordings in cats, that not long after retinal lesions a wave of hyperactivity shifts from the border of the unaffected cortex into the LPZ, and that during the course of the recovery, hyperactive cells inside the LPZ develop ectopic receptive fields and regain orientation selectivity. Some functional changes driven by the lesion such as the increase in RF size and the hyperactivity tend to normalize at longer periods after the lesion. However, the orientation tuning of cells located inside the LPZ became broader, and this effect remained even one year after the lesion. One possible explanation for the changes in receptive field size over time comes from the changes in activation rates. They propose a mechanism by which the imbalance between inhibition and excitation could favor synaptic plasticity. The conjunction of lateral excitation and disinhibition could allow neurons located in the LPZ to become excited by formerly sub threshold inputs and give rise to the newly formed receptive fields observed after the lesion (Hübener and Bonhoeffer [43]).

The first characterization of the structural changes induced by retinal lesions was done by Darian-Smith and colleagues (Darian-Smith and Gilbert [16]) who injected biocytin at the border of the LPZ of binocularly lesioned cats and, at different time points after the lesion (2 weeks, 1 month and 1 year), measured the densities of axons projecting into the LPZ and into adjacent cortex as a control. They reported not only nearly a doubling in the number of axonal processes into the LPZ compared to control regions, but also implied the possibility of a doubling on the number of axonal boutons given that bouton densities did not differ from control cortex.

New imaging technologies, such as two-photon microscopy (Trachtenberg et al. [78], Holtmaat et al. [37]), allowed a finer and more detailed characterization of the structural underpinnings of adult plasticity in the visual cortex. Yamahachi et al. [83] showed in monkeys that, in contrast to baseline conditions, where axons were found to be conspic-

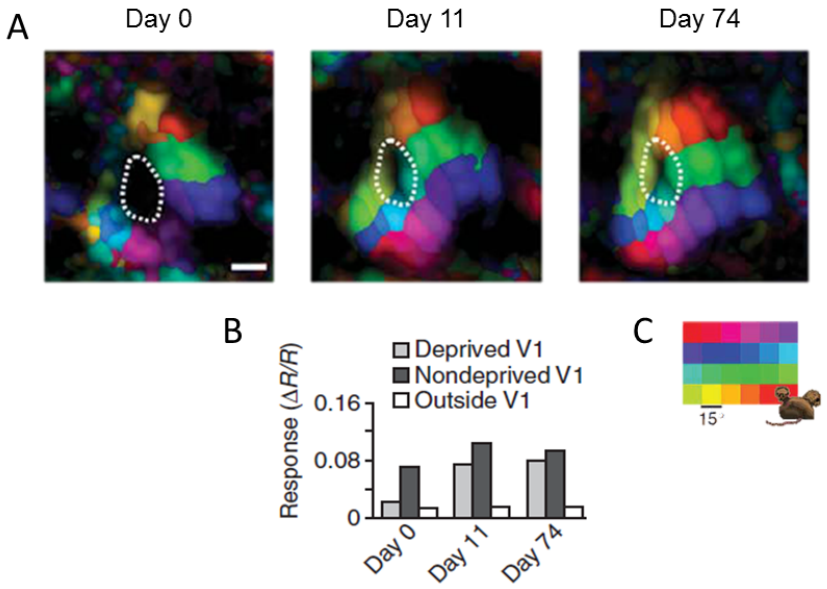

Figure 1.2.2 – Extent of functional recovery in mouse visual cortex after retinal lesions; adapted from Keck et al. [47]. (A) Color-coded retinotopic maps of activity at several time points after retinal lesions showing the extent of the "filling-in". Scale bar: 700µm. Dashed line: outline LPZ. (B) Comparison of average intrinsic responses inside the initially deprived (light gray) and in non deprived (dark gray) regions of the visual cortex and outside (white) of the visual cortex (C) Layout of drifting grating stimuli (6x4 grid comprising 90x60 degrees of visual space) used for mapping retinotopy. Reprint permission: 3666990602343

uously stable (Stettler et al. [74]), during the first 2 weeks after retinal lesions there was a high degree of axonal plasticity, with a large number of new branches forming inside the LPZ. Despite pruning during the subsequent month, which decreased the number of axonal branches in the LPZ, the overall number of axons remained higher than prior to the lesion, in accordance with the previous report by Darian-Smith and Gilbert [16].

It was not until 2008 that Keck et al. [47] investigated adult plasticity in mouse visual cortex using partial retinal lesions. Optic imaging of intrinsic signals proved that the "filling-in" also takes place in mice similarly as in cats and monkeys, except that in mice the "filling-in" comprises the whole of the LPZ so that, in the end, visual responses are almost completely recovered. This is probably mainly due to differences in the architecture of the visual system of mice in comparison to monkeys/cats. Mice have a relatively small visual cortex in comparison to the extent of the dendritic trees and corresponding axonal arbors and on the other hand, the magnification factor (degrees visual space/unit

distance in visual cortex) is much smaller than in the other model systems. Therefore, a single dendritic tree could easily extend over the whole LPZ in a mouse and provide better reach to input outside the deprived region allowing for the complete “filling-in” to take place.

The study by Keck et al. [47] not only provided functional data, by taking advantage of two-photon microscopy, it also provided evidence for structural changes of dendritic spines. Specifically, they observed that soon after retinal lesions, spine turnover on the apical tufts of layer 5 cells inside the LPZ was nearly three times larger than in unlesioned controls leading to a nearly entire exchange of spines in the deprived cortex after two months. This high level of structural plasticity, though surprising by its magnitude, correlates well with the aforementioned degree of recovery found in this paradigm in mice.

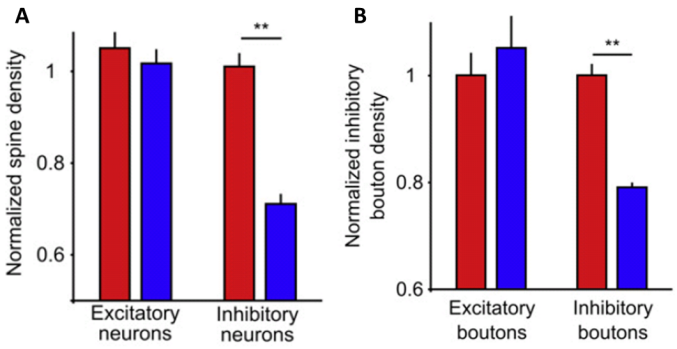

Figure 1.2.3 – Structural changes to inhibitory neurons after retinal lesions; adapted from Keck et al. [48]. Red: control; Blue: retinal lesions. (A) Spine density remains constant in excitatory cells after 72h but drops on inhibitory neurons (B) Bouton density 72h after retinal lesion is decreased in inhibitory neurons but is not changed in excitatory cells. Reprint permission 3666990820345

Recently, structural changes of inhibitory cells after retinal lesions have been investigated. In a later study, Keck et al. [48] reported a fast and sustained reduction in the number of dendritic spines as well as a sharp drop in bouton density of inhibitory neurons in the LPZ (see figure 1.2.3). This finding implies that, as a consequence of sensory deprivation, the excitatory input to inhibitory neurons decreases, which in turn would decrease their synaptic output, resulting in an overall disinhibition that could facilitate the subsequent functional reorganization. Last year, Marik et al. [59] found that under normal conditions inhibitory axons in monkeys are very stable, corrob-

orating Stettler et al. [74], but that after a retinal lesion inhibitory axons within the LPZ undergo significant growth and pruning, with the direction of growth pointing towards the LPZ border. In spite of the increased spatial extent of these inhibitory arbors, sometimes even reaching to the peri-LPZ, their density decreases. For cells located in LPZ border regions the growth rate was slower and dependent on distance from the LPZ, with cells farther from it experiencing more axonal growth directed towards the peri-LPZ but, interestingly, never going beyond the LPZ border. The authors hypothesize that inhibitory axons extending beyond the LPZ/peri-LPZ border might target the peri-LPZ excitatory neurons that send the horizontal projections into the LPZ and account for the necessary re-balance of excitatory-inhibitory input during the later stages of the functional recovery.

Against the wealth of studies that found cortical reorganization after retinal lesion (Kaas et al. [45], Gilbert and Wiesel [30], Darian-Smith and Gilbert [17], Calford et al. [13], Giannikopoulos and Eysel [24], Keck et al. [47], Palagina et al. [65], Yamahachi et al. [83]) Logothetis and colleagues (Smirnakis et al. [71]) presented a set of controversial results which have been a matter of debate in the field (Calford et al. [12], Giannikopoulos and Eysel [24], Palagina et al. [65], Botelho et al. [11]). Using a combination of fMRI and electrophysiology in macaque monkeys to record activity in the LPZ over many months, Smirnakis et al. detected little evidence for functional recovery. Recently, another fMRI study with human patients of macular degeneration found similar negative results (Baseler et al. [5]). Nevertheless, other fMRI studies have found reorganization after retinal lesions (Baker et al. [4, 3]). The reason for these contradictory findings might relate to species and methodological differences. For instance, Calford et al. [12] argue that fMRI is not the appropriate technique to study spiking activity. Moreover, Abe et al. [1] found differences between spiking and LFP (local field potential) activity before and after retinal lesions. Although at baseline the two measurements show similar tuning to stimulus positions, after the lesion LFP power is reduced and its positional tuning barely apparent. Since fMRI signals have a stronger relationship with LFPs than with spiking this could therefore be a possible reason for the discrepancy.

1.3 Two-photon microscopy and calcium indicators

Two-photon calcium imaging has become a powerful tool to investigate neuron function *in vivo* for a number of reasons. On one hand, two-photon microscopy (Denk et al. [19], Helmchen and Denk [33]) is based on the use of infrared laser light for the excitation of fluorophores, which in itself has several advantages: first, fluorophore excitation is restricted to the beam's focus where photon density is high enough to produce excitation, restricting therefore the out-of-focus excitation typical of confocal microscopy; second, the longer wavelength of the excitation beam allows deeper tissue penetration due to less scattering and reflection, making it possible to image beyond 450μm depth in the cortex. And third, photo toxicity and bleaching are minimized by the pulsed laser light.

Fluorescent calcium indicators respond to the increase in intracellular calcium levels produced by the calcium influx triggered by neuronal firing by modulating their fluorescence intensity accordingly (Tsien and Tsien [79], Berridge et al. [8]). Typically, the fluorescence change of this type of indicators is greater than that of voltage sensitive dyes (Orbach et al. [64]) and therefore more appropriate for *in vivo* imaging despite the fact that the latter provide a more direct read-out of neuronal activity (Stosiek et al. [75], Tian et al. [77, 76], Chen et al. [14]).

Two-photon calcium imaging is advantageous to study cell function for a variety of reasons. In contrast to intrinsic imaging that allows population imaging but lacks single-cell resolution and to electrophysiology which provides a very accurate activity read-out but is restricted to a handful of active or putative single units, two-photon calcium imaging permits the recording of the activity of large neuronal populations with single-cell spatial and near-spike temporal resolution. However, one disadvantage to take in consideration are the non-linearities of the fluorescence change of the calcium indicators in response to neuronal activity which make spike detection less reliable than electrophysiological recordings (Hendel et al. [34], Grewe et al. [31]).

Calcium imaging was key to this study. When coupled with an structural indicator (mRuby)

the genetically-encoded calcium indicator GCaMP6s (Chen et al. [14]) allowed the re-identification of the same neurons on each of the subsequent imaging sessions over the whole of the experimental series, allowing for chronic imaging of the same neuronal population over weeks and months. Calcium imaging also has the advantage that all cells within an optical section can be morphologically detected, regardless of their activity levels, therefore silent and non-responsive cells are not excluded from the analysis as would happen with electrophysiology, allowing for a better estimation of general activity levels.

For this study, I employed both synthetic and genetically-encoded calcium indicators. On a first approach I used OGB1-AM, a synthetic indicator that could not be used for chronic imaging, but that had, however, been previously reported to accurately detect single receptive fields in mouse visual cortex (Smith and Häusser [72], Bonin et al. [10]). Later, the development of the genetically-encoded calcium indicator GCaMP6s (Chen et al. [14]), which Tobias Rose (MPI of Neurobiology, Dept. Synapses-Circuits-Plasticity, Martinsried, Germany) coupled to a structural indicator (mRuby), allowed to fulfill the initial aim of this project and image the same neuronal populations chronically after retinal lesions.

1.4 Aims of the study

The main aim of the present study was to investigate adult functional plasticity in mouse visual cortex at the single cell level. For that purpose, I have made use of the long established retinal lesion model of adult plasticity. Although much is known about the process leading to the cortical recovery of visual properties, at present the detailed cellular mechanisms of these reorganization processes are not well understood. While previous intrinsic signal imaging data clearly showed reorganization in adult mouse visual cortex (Keck et al. [47]), this method did not allow following how individual neurons regain responsiveness to visual stimuli and how their receptive fields change over time. Giannikopoulos and Eysel [24] already tried to tackle this problem by single-cell electrical recordings in cat visual cortex in 2006. More recently, Abe et al. [1] has attempted chronic recordings in macaque monkeys with micro-electrode arrays. However, extracellular recordings have the limitation that they do not allow to follow chronically exactly the same neurons over time, even if the recording positions with arrays are more stable. Moreover, these type of recordings are restricted to active neurons.

Therefore, in order to follow the functional reorganization of the visual cortex at the level of individual neurons, I used chronic two-photon calcium imaging.

First, I characterized the changes in receptive field size and position triggered by the retinal lesion. In view that, in all studies to date, a shift in receptive field size position towards the outside of the LPZ, as well as a significant increase in size in the initial stages after RL that decreases in subsequent stages of the recovery, have been reported.

Second, I sought to determine if retinal lesions produce differences in general activity levels, and whether this effect has a distance correlation to LPZ position, since it has been reported that in the initial stages of the recovery there is a wave of hyperactivity migrating from the border to the inside of the LPZ that subsides over longer recovery times (Giannikopoulos and Eysel [24], Palagina et al. [65]).

Last, I looked for effects on orientation tuning, and whether changes to this property also

differed in a spatial fashion given that Giannikopoulos and Eysel [24] reported an increase in tuning width for cells inside the LPZ, an effect that still remained even one year after the lesion.

2

Material and Methods

2.1 Methods

All experimental procedures were carried out in compliance with institutional guidelines of the Max Planck Society and the local government (Regierung von Oberbayern). All experiments were performed using female C57/Bl6 mice aged between postnatal day (p) 30 and p140. Materials appear referenced by an alphanumeric subscript in the method description. For a comprehensive list see separate section below.

2.1.1 Surgical procedures

Depending on the type of experimental approach used to measure single cell activity in primary visual cortex (V1), either acute (see section 2.1.1.1) or chronic 2-photon imaging (see section 2.1.1.2), a different kind of surgery was performed. The first type employs a synthetic calcium indicator and allows for a one-time-only imaging experiment, whereas the latter uses viral expression of genetically-encoded calcium indicators, such as GCaMP6s, and permits long time characterization of response properties.

2.1.1.1 Acute experiments using a synthetic indicator

Mice ((p) 30 – 70) were anesthetized by intraperitoneal injection with a mixture of Fentanyl$_{A.1}$(0.05 mg/kg), Midazolam$_{A.2}$ (5.0 mg/kg), and Medetomidin$_{A.3}$ (0.5 mg/kg). Anesthesia levels were maintained by re-injection of one-fifth of the initial dose after two hours. To prevent eye dehydration during surgery, a thin layer of cream$_{A.4}$was applied at the beginning of surgery. After attaching a headplate$_{B.1}$ to the skull, the cortical surface was exposed by a craniotomy, thereafter it was maintained moist with artificial cerebrospinal fluid (ACSF; 125 mM NaCl, 5 mM KCl, 10 mM glucose, 10 mM HEPES, 2 mM $MgSO_4$, and 2 mM $CaCl_2$ [pH 7.4]). The calcium-sensitive dye Oregon Green 488 BAPTA-1, AM$_{A.5}$ (OGB1-AM) was dissolved in 4 ml DMSO containing 20% pluronic acid$_{A.6}$, and further diluted (1/11) in dye buffer (150 mM NaCl, 2.5 mM KCl, and 10 mM HEPES [pH 7.4]) to a final concentration of around 0.9 mM. Dye solution was pressure injected into the visual cortex at a depth of 200 – 300 μm with a micropipette$_{B.2}$ (3 – 5 MΩ, 0.55 – 0.83 bar, 2 – 3 min). After dye injection, the cortex was covered with 2% agarose$_{A.7}$ in saline$_{A.8}$ and a coverslip$_{B.3}$. Immediately thereafter, two-photon calcium imaging was started (see section 2.1.5).

2.1.1.2 Virus injection and chronic window implantation

This procedure was performed following a protocol modified from Holtmaat et al. [36]. Mice (around p50) were anesthetized by intraperitoneal injection with a mixture of Fentanyl$_{A.1}$ (0.05 mg/kg), Midazolam$_{A.2}$ (5.0 mg/kg), and Medetomidin$_{A.3}$ (0.5 mg/kg) and placed in a stereotactic apparatus. To prevent eye dehydration during surgery, a thin layer of cream$_{A.4}$was applied. After applying a local anesthetic (lidocaine$_{A.9}$), the skin over the head was removed from the skull with scissors$_{B.4}$. Next, the skull was disinfected with iodine solution$_{A.10}$, cleared of hairs and roughened with a scalpel$_{B.5,\ B.6}$. Finally, before the craniotomy, the edges of the exposed skull were sealed with Histoacryl$_{C.1}$. Using a drill$_{B.7,B.8}$ a 5mm Ø craniotomy located over the left hemisphere in primary visual cortex

was performed. Once the bone lid had been removed, the brain was kept moist with ACSF (125 mM NaCl, 5 mM KCl, 10 mM glucose, 10mMHEPES, 2 mM $MgSO_4$, and 2 mM $CaCl_2$ [pH 7.4]), blood from meningeal vessels was removed with $Sugis_{B.9}$ until the bleeding stopped. A $micropipette_{B.10}$(5 – 8 MΩ) connected to a $pressure\ injector_{D.1}$and mounted to a $micromanipulator_{D.2}$, was used to inject a total volume of about 600nl of the $virus_{E.1}$ solution (AAV1.hSyn1.mRuby2.GSG.P2A. GCaMP6s.WPRE. SV40, titer: 3.73*e+13 GC/ml). The virus was injected successively up to a depth of about 350 µm below the cortical surface in monocular V1 at a rate of 5-10nl/s. Injections were placed in three or four different locations. After virus injection, a $cover\ slip_{B.3}$, affixed with $dental\ cement_{C.2}$, sealed the craniotomy. A custom-made metal $headbar_{B.11}$(oval plate, 8 mm Ø opening, two screw notches) was mounted on the skull with $cyanoacrylate\ glue_{C.3}$ and the space between skull and $headbar_{B.11}$ as well as any remaining exposed skull was covered with $dental\ cement_{C.2}$. An intraperitoneal injection of a mixture of the opioid receptor antagonist $Naloxone_{A.11}$(1.2 mg/kg), the GABA-A receptor antagonist $Flumazenile_{A.12}$(0.5 mg/kg) and the α2 adrenergic receptor antagonist $Atipamezole_{A.13}$(2.5 mg/kg) reverted anesthesia. To ease pain the analgesic $Carprofen_{A.14}$(4.0 mg/kg) was injected subcutaneously. During recovery from anesthesia (ca. one hour) mice were kept under a $heat\ lamp_{B.12}$.

2.1.2 Retinal lesions

Retinal lesions were carried out in collaboration with Ulf Eysel (Ruhr University, Bochum, Germany). Mice were anesthetized by intraperitoneal injection with a mixture of $Fentanyl_{A.\ 1}$ (0.05 mg/kg), $Midazolam_{A.2}$ (5.0 mg/kg), and $Medetomidin_{A.3}$ (0.5 mg/kg) and the pupil of the right eye dilated with a few drops of $Atropine_{A.15}$(0.01%). The procedure by which the retina was focally photo-coagulated with multiple confluent lesions (300 mm, 500–600 mW, 200 ms) through a laser-adapted operating microscope, followed the protocol given in Keck et al. [47], with lesions located in the dorso-temporal retina, close to the optic disc and of a relative size of approximately 20° in visual space.

2.1.3 Retina staining

To demonstrate the extent of the lesions to the retina, animals were anesthethized by intraperitoneal injection with a mixture of Fentanyl$_{A.1}$ (0.05 mg/kg), Midazolam$_{A.2}$ (5.0 mg/kg), and Medetomidin$_{A.3}$ (0.5 mg/kg) before PFA perfusion, subsequently eyes were removed and fixed in PFA. With the help of Irene González-Menéndez (Institute for Ophthalmic Research, Tübingen, Germany) retinas from lesioned and control eyes were removed and mounted for staining. After dehydration the tissue was stained with a cresyl violet solution. Images were taken with a Zeiss Stereo Microscope$_{D.3}$in bright field mode.

2.1.4 Optical Imaging of Intrinsic Signals (OI)

The following procedure was performed following a protocol adapted from Schuett et al. [70]. After window implantation (see section 2.1.1.2), animals were lightly anesthetized by intraperitoneal injection with a mixture of Fentanyl$_{A.1}$ (0.025 mg/kg), Midazolam$_{A.2}$ (2.5 mg/kg), and Medetomidin$_{A.3}$ (0.25 mg/kg). Once sedated, mice were placed over a heating blanket$_{D.4}$ and their heads fixed to the imaging setup using the metal headbar's$_{B.11}$ lateral fixation points. The eye ipsilateral to the craniotomy was covered with eye cream$_{A.4}$, while the contralateral eye was kept moist with eye drops$_{A.16}$. Visual stimuli consisted of 25 patches (15x15 deg of visual angle) of square wave gratings moving in 8 orientations (spatial frequency: 0.04cpd, temporal frequency: 2cps) presented in a random order for 0.38s/each. These square-shaped stimuli were presented in a random order at the different positions (seven columns and five rows of stimuli). Each 10 sec stimulus presentation at one position was followed by a blank screen for 4 sec. The whole stimulus sequence was repeated five times. To image the bloodvessel-pattern, the cortex was illuminated with monochromatic light of 525nm$_{F.1}$. For mapping retinotopy, illumination from a halogen lamp was changed to 712nm$_{F.2}$ and images were collected with a CCD camera$_{F.3}$ focused around 500 microns below the pial surface. All images were acquired using a 5x microscope objective$_{F.4}$. Acquisition and analysis software were custom written in

Matlab$_{H.1}$. Stimuli were also generated in Matlab using the Psychophysics Toolbox$_{H.2}$ extension. Stimuli were presented on a 20" LCD monitor$_{D.5}$ which was curvature and gamma corrected and with its luminance adjusted to half-maximum. This screen was placed at a 45 degree angle to the mouse's body at a distance of 10cm.

2.1.5 Two-photon calcium imaging

In calcium imaging experiments using OGB1-AM, cells were imaged at several depth levels, between 120 μm and 250 μm below the pial surface in monocular V1. Using a custom built two-photon laser scanning microscope equipped with a MaiTai HP DeepSee femtosecond laser$_{G.1}$ and a 40x water immersion objective$_{G.2}$ (0.8 NA), a 210μm x 125μm field of view was scanned at 20 Hz and 671 x 400 pixel resolution. OGB1-AM was excited at 830 nm. The emitted light was detected through a 525/50 nm bandpass filter$_{G.3}$. For repeated calcium imaging experiments using the genetically-encoded calcium indicator GCaMP6s-mRuby, neurons were imaged with a 16x water immersion objective$_{G.4}$ (0.8 NA) in several regions throughout layer 2/3 in monocular V1 (130 μm -180 μm depth). In these experiments both GCaMP6s and mRuby were excited at 930nm. Emitted light from GCamP6s was detected through a 525/50nm bandpass filter$_{G.3}$whereas mRuby was detected through a 607/70nm$_{G.5}$. A 325μm x 173μm field of view as scanned at 60 Hz at 671 x 400 pixel resolution. Acquired images were binned on writing to disc to a final frame rate ranging between 5.4-6Hz. Custom developed software (Colibri$_{H.3}$ written in LabView$_{H.4}$ by Max Sperling) was used both for microscope control and image acquisition. Eye and pupil position were monitored at all times during data acquisition.

2.1.6 Visual stimuli

All visual stimuli were programmed with Matlab using the Psychophysics Toolbox$_{H.2}$ extension.

2.1.6.1 Orientation tuning

To characterize orientation and direction tuning, full field, moving square-wave gratings at 16 orientations (22.5°-360°) were used. In OGB1-AM experiments moving gratings and gray screen were shown for 3 seconds each, the spatial frequency was 0.03cpd and the temporal frequency was 1.5cps. In experiments using a genetically-encoded indicator, settings were slightly different: gratings had a spatial frequency of 0.04cpd and a temporal frequency of 2cps and were shown during 2.5 seconds followed by a gray screen for 4 seconds. Spatial and temporal frequency of the stimuli were chosen to optimize cell's responses depending on the experimental conditions. In both cases, each stimulus block started with the gray screen and was repeated five times.

2.1.6.2 Receptive field mapping

To determine receptive field position and discriminate between ON and OFF subfields, square black or white patches (10°x10°) displayed over an isoluminant gray background were shown alternatively in a random fashion at 70 different positions covering a total of 100°x70° (10 columns and 7 rows). To avoid successive stimulation of neighboring areas of the visual field that might cause response inhibition or receptive field detection errors, a constraint was introduced to the randomization of the stimulus presentation. Stimulus presentation lasted 0.7 seconds and was almost immediately followed (inter stimulus interval 0.1 seconds) by another stimulus at a distant position. Each position was covered twice per stimulus block (once white, once black), and blocks were repeated fifteen times. To improve receptive field detection, the overall stimulation area was positioned according to the retinotopic map determined previously by OI for each imaging region. For OGB1-AM experiments the stimulus was similar, except that it consisted only of either 16 (25°x25°) or 24 patches (15°x15°) covering a total of 90°x60°, the presentation time of the stimulus was 3.5 seconds, and the inter stimulus interval was 5 seconds. Stimuli were presented pseudo-randomly in this case and repeated three times in total.

2.1.7 Data analysis

2.1.7.1 Cell detection

Data were analyzed using $\text{Matlab}_{\text{H.1}}$. Image sequences were full-frame corrected for tangential drift and small movements caused by heart beat and breathing. Recordings with significant brain movements or vertical drift were excluded from further analysis. In experiments with the synthetic indicator OGB1-AM, cell body detection was based on the OGB1-AM staining itself, derived from an average morphological image (7092 frames). For GCaMP6s experiments, cell body detection was based on the overlay of the structural channel (mRuby) and the activity channel (GCaMP6s) and derived from an average morphological image (3034 or 7644 frames). In both cases, neuronal cell bodies were detected semi-automatically as regions of interest using a set of morphological filters for cell intensity, size, and shape, and subsequently confirmed by visual inspection. Cells were manually re-identified in subsequent imaging sessions and annotated for further analysis.

2.1.7.2 Trace extraction

Average fluorescence of the area within the cell body was calculated per frame, resulting in a timeline of mean absolute cell body fluorescence for each neuron. Cell traces were red-channel corrected for small drifts of the signal (only in GCamP6s data) and smoothed using a moving sliding window (kernel size=7) and neuropil subtracted (neuropil factor=0.7, Kerr and Denk [50]) before further analysis.

2.1.7.3 Analysis of orientation and direction tuning

Fluorescence responses to each grating direction were calculated per trial as $\Delta F/F$ taking the previous gray period as a baseline. Cells were considered responsive if the response to any of the stimuli was significantly different from baseline (ANOVA at $p < 0.05$). Cells were considered orientation selective if the response to at least one of the 16 direc-

tions was significantly different from the response to all other directions (ANOVA at p < 0.05). In pixel-based activity maps (HLS maps), hue (H) represents preferred orientation or direction, lightness (L) response amplitude and saturation (S) indicates tuning width. Bandwidth was calculated after smoothing with a moving average filter (kernel size: 5) on raw-data tuning curves and was defined as the half-width of the tuning curve at $1\sqrt{2}$ times the maximum response in degrees, calculated using interpolation (Ringach et al. [67]). Similarly, the orientation selectivity index (OSI) was calculated from raw-data tuning curves as in Ringach et al. [67]. Preferred movement direction ($\vartheta_{\mathrm{PREF}}$) was determined by fitting the average responses over all directions with a two-peaked 360° wrapped Gaussian function (Li et al. [54]). Where R_{OFFSET} is the baseline fluorescence, R_{PREF} is the response to the preferred direction θ_{PREF}, R_{OPP} is the response to the opposite of the preferred direction (θ_{PREF} + 180°), σ is the SD of the fitted Gaussian functions and the function y = ang(x) wraps the angular difference x = θ– θ_{PREF} on an interval between 0° and 180°:

$$R_\theta = R_{OFFSET} + R_{PREF} \cdot e^{\frac{-(ang(\theta-\theta_{PREF})^2}{2\sigma^2}} + R_{OPP} \cdot e^{\frac{-(ang(\theta+180-\theta_{PREF})^2}{2\sigma^2}}$$

2.1.7.4 Analysis of receptive field structure and position

Since stimuli were continuously presented in experiments using genetically-encoded calcium indicators, ΔF/F was calculated using as baseline the median of the 10$^{\mathrm{th}}$ to the 70$^{\mathrm{th}}$ percentile of each cell's activity trace. This provided the estimation of baseline activity throughout the recording, since there were no inter-stimulus intervals from which to draw baseline activity as in orientation tuning experiments. Afterwards traces were sorted according to stimulus position and contrast (black or white) and averaged over all repeats. To minimize the contribution of noise and spontaneous activity to the signals, data from trials deviating maximally from the mean were excluded (final number of trials analyzed: thirteen). For a set time window (7x stimulus presentation time: 1x before stimulus onset, 6x after) response latency was defined as the first imaging frame after stimulus onset for which there was a significant difference (ANOVA at p < 0.05) in activity levels among

all positions. Cells were considered significantly responsive if such a value was found. All traces were averaged in time bins equal to stimulus presentation length, interpolated into a 1°x1° grid, Z-scored and thresholded (2SD). After applying a gaussian filter (kernel size 5) to the data, and selecting the time bin corresponding to the latency, a receptive field was defined and its properties determined. Receptive field center was defined as the center of mass, whereas perimeter and size were respectively derived from pixel summations on the border or the whole of the receptive field area previously defined.

Since varying noise levels and/or spontaneous activity could cause erroneous detection of receptive fields, subsequent visual inspection was conducted to improve on accuracy. At baseline, receptive fields could be accurately defined for approximately 40% of cells morphologically identified in each field of view.

2.1.7.5 Group data analysis

Mice were imaged repeatedly over a two month period after retinal lesions, with imaging sessions more closely spaced in the first weeks after sensory deprivation (daily recordings from day 1-day 7 post-lesion; every five days from day 10-day 30 post-lesion; weekly from day 37-day 65 post-lesion). There were up to three baseline imaging sessions before retinal lesions.

Two spatially defined regions based on relative distance to the LPZ were defined for analysis: the first, far, including cells located more than 350µm away from the center of the LPZ (4 mice, 4 imaging planes, 60 cells) and the second, close, including those in its surroundings, 100µm-200µm away (4 mice, 6 imaging planes, 70 cells)

For the analysis of changes in receptive field parameters and orientation tuning after retinal lesions, only cells for which a RF could be detected in at least at one baseline imaging session and at least 4 other sessions after lesion induction were included (~55%cells in far, ~40% in close).

Data obtained after lesion induction was split in three different time bins: the first time-bin comprised the first two weeks after the lesion, that is datapoints from days 1-10 post-

lesion (early), the second the next two weeks and therefore up to a month after the lesion (intermediate) and the last, from one up to two months after (late) lesion induction. Data included in each of these bins was the result of averaging over the available data at all time points belonging to a bin.

To analyze shifts in RF position, the euclidean distance between the RF centers at baseline and the average (geometric median) position at each of the three time bins after the lesion was calculated.

The direction of the shift was calculated by vector analysis over all receptive field centers for four close regions from all four mice included in the dataset using the MatLab tools for circular analysis described in Berens [7].

RF size was calculated as the average at each time-bin for each group (far vs close). Differences to baseline were normalized and expressed as percent change for each time-bin.

Differences in total evoked activity levels were determined by averaging the responses of all cells identified at each time-point at the onset of the moving grating stimulus. A total of ~200 cells per group from three mice was used for this analysis. One mouse was excluded from this type of analysis due to low expression levels of the genetically-calcium indicator at baseline causing a marked decrease of total evoked activity levels that rendered this dataset useless for later comparison.

For the analysis of the stability of orientation selectivity (OSI > 0.5) over time (before and at the three time bins after lesion induction) cells were classified as *always selective*, if they were selective throughout or *never selective* if the opposite was true. Cells orientation selective at baseline that lost their selectivity at any time point after the lesion were classified as *selectivity loss,* whereas the group *selectivity gain* was defined as not being selective at baseline but becoming selective afterwards. *Unstable selectivity* describes all cells that do not fit in any of the aforementioned categories and for which orientation selectivity is alternatively gained, lost or recovered at different time points.

Changes in bandwidth and preferred orientation with respect to baseline were calculated

for those cells that were orientation selective at baseline, i.e. belonging to the *always selective*, *unstable selectivity* (but selective at baseline) and *selectivity loss* groups. For these cells, the mean absolute shift from preferred direction (PrefDir) and preferred orientation (PrefDir) was calculated at each time-bin as well as the mean bandwidth before and after the lesion at each time-bin.

To analyze the amplitude of responses at PrefOri, for each cell and time-bin, including baseline, the average amplitude at PrefOri was calculated and then averaged for all cells orientation selective at baseline in each region to obtain the mean of the whole population.

2.1.7.6 Statistics

For statistical analysis, all datasets were tested for homogeneity of variance (Levene Test) and for normal distribution (Kolmogorov-Smirnov Test). For analyses where these assumptions were not true, non-parametric tests were used, either a Mann Whitney U-Test or a Willcoxon sign-rank Test, depending on the comparison: A Mann Whitney U-Test was applied to comparisons between regions at each of the different time-bins, while a Willcoxon sign-rank test was used for intra-group comparisons over the time dimension (multiple measures test). In all cases a Bonferroni correction for multiple comparisons was further applied post-hoc. To discard the contribution to the effect of variations in the data from different animals, a further analysis of variance (ANOVA) was performed.

2.2 Materials

In order of appearance in the methods section.

2.2.1 Chemicals, drugs and similar

A.1 Fentanyl, HEXAL AG (Holzkirchen, Germany)

A.2 Dormicum ® V (Midazolam), Roche Pharma AG (Grenzach-Wyhlen, Germany)

A.3 Dormitor ® (Medetomidine), Janssen Animal Health (Beerse, Belgium)

A.4 Isopto-Max eye lubricant, Alcon Pharma GmbH (Freiburg, Germany)

A.5 Oregon Green ® 488 BAPTA-1, AM, 50 μg, Life Technologies GmbH (Darmstadt, Germany)

A.6 Pluronic ® F-127 20% solution in DMSO, Life Technologies GmbH (Darmstadt, Germany)

A.7 Agarose, Biomol GmbH (Hamburg, Germany)

A.8 Isotone Kochsalzlösung 0.9% Braun, B. Braun Melsungen AG (Melsungen, Germany)

A.9 Xylocain ® Pumpspray, AstraZebeca GmbH (Wedel, Germany)

A.10 Braunol ® 7.5 (Iodine solution), B. Braun Melsungen AG (Melsungen, Germany)

A.11 Naloxon-hameln (Naloxone), Hameln Pharmaceuticals GmbH (Hameln, Germany)

A.12 Anexate ® (Flumazenile), Roche Pharma AG (Grenzach-Wyhlen, Germany)

A.13 Antisedan ® (Atipamezole), Pfizer Animal Health (Madison, New Jersey, USA)

A.14 Rimadyl ® (Carprofen), Pfizer Animal Health (Madison, New Jersey, USA)

A.15 Atropin EDO (Atropinsulfat 0.5%), Dr. Mann Pharma (Berlin, Germany)

A.16 Oculotect ® fluid sine 50 mg/ml PVD Augentropfen, Novartis Pharma GmbH (Melsungen, Germany)

2.2.2 Solutions

All components of the following solutions were from Sigma-Aldrich (St. Louis, Missouri, USA)

2.2.2.1 Artificial Cerebrospinal Fluid (ACSF)

125 mM NaCl

5 mM KCl

10 mM Glucose*H2O

10 mM HEPES 2 mM CaCl2*2H2O

2 mM MgSO4*7H2O

ASCF was adjusted to pH 7.4 with 1 N NaOH and sterile filtered.

2.2.2.2 Dye buffer

150 mM NaCl

2.5 mM KCl

10 mM HEPES

The buffer was adjusted to pH 7.4 using 1 N NaOH and sterile filtered.

2.2.2.3 Paraformaldehyde (PFA)

4% paraformaldehide

0.1M PBS

2.2.2.4 Cresyl Violet

1g Cresyl Violet

0.25g CH_3COONa

3.1ml CH_3COOH

distilled H_20 to 100ml

2.2.3 Tools

B.1 Headplate (chamber type, 46 x 14 mm, metal), Max Planck Institute machine shop (Martinsried, Germany)

B.2 Borosilicate glass capillaries GC150F-10, Harvard Apparatus (Holliston, Massachusetts, USA)

B.3 Deckgläser rund 5 mm, Menzel GmbH (Braunschweig, Germany)

B.4 Hardened Fine Iris Scissors, 8.5 cm, straight, Fine Science Tools GmbH (Heidelberg, Germany)

B.5 Scalpel blades #11, Fine Science Tools GmbH (Heidelberg, Germany)

B.6 Scalpel handle #7, Fine Science Tools GmbH (Heidelberg, Germany)

B.7 K.1070 High Speed Rotary Micromotor Kit, 2.35mm, Foredom Electric Co. (Connecticut, USA)

B.8 Drill bits HP-1004, Hager & Meisinger GmbH (Neuss, Germany)

B.9 Sugi®, Kettenbach Medical (Eschenburg, Germany)

B.10 Borosilicate glass capillaries 1408472, Hilgenberg GmbH (Germany)

B.11 Headbar (chamber type, 24 x 10 mm, metal), Max Planck Institute machine shop (Martinsried, Germany)

B.12 Heatlamp, Glamox Luxo GmbH (Bremen, Germany)

B.13 Cotton tips, 15 cm, medical care & serve® (Wurmlingen, Germany)

B.14 Dumont #7 Forceps, standard, Fine Science Tools GmbH (Heidelberg, Germany)

B.15 Injekt®, B. Braun Melsungen AG (Melsungen, Germany)

B.16 Introcan®, B. Braun Melsungen AG (Melsungen, Germany)

B.17 Omnican®, B. Braun Melsungen AG (Melsungen, Germany)

B.18 Sterican®, B. Braun Melsungen AG (Melsungen, Germany)

2.2.4 Dental cement and glues

C.1 Histoacryl ®, Aesculap AG (Tuttlingen, Germany)

C.2 Paladur ®, Heraeus Kulzer GmbH (Hanau, Germany)

C.3 Pattex ® BlitzKleber gel, Henkel CEE GmbH (Wien, Austria)

2.2.5 Instrumentation

D.1 TooheySpritzer Pressure System IIe, Toohey Company (Fairfield, New Jersey, USA)

D.2 Micromanipulator MO-10, Narishige (Tokyo, Japan)

D.3 Zeiss Stereo Lumar V.12, Zeiss (Germany)

D.4 Homeothermic blanket with rectal probe, Harvard Apparatus (Holliston, Massachusetts, USA)

D.5 TFT monitor 20”, Dell GmbH (Frankfurt am Main, Germany)

D.6 AxoClamp 2B, Molecular Devices (Sunnyvale, California, USA)

D.7 Digital storage oscilloscope Classic 5000, Gould Electronics GmbH (Eichstetten, Germany)

D.8 Operationsmikroskop SOM-62, Karl Kaps GmbH (Aßlar, Germany)

D.9 Stimulator Master-8, A.M.P.I. (Jerusalem, Israel)

D.10 Two-step vertical puller P-10, Narishige International Limited (London, UK)

2.2.6 Virus

E.1 AAV1.hSyn1.mRuby2.GSG.P2A.GCaMP6s.WPRE.SV40, designed by Tobias Rose PhD (unpublished) produced at University of Pennsylvania Vector Core Services(Philadelphia, Pennsylvania, USA)

2.2.7 OI components

F.1 Emission filter 525/50 nm bandpass filter, AHF Analysetechnik (Tübingen, Germany)

F.2 Emission filter 712/10 nm bandpass filter, AHF Analysetechnik (Tübingen, Germany)

F.3 CCD Dalstar 1M60 60fps 1kx1k, Dalstar (Waterloo, Canada)

F.4 Zeiss Plan-NEOFLUAR 5x/0.15na Objective, Zeiss (Germany)

F.5 Power Source Lambda UP20-10, Megown Test & Measurement Inc. (USA)

F.6 Halogen lamp, Spindler&Hoyer, nr.030125 (Germany)

2.2.8 Two-photon microscope components

G.1 MaiTai HP DeepSee, SpectraPhysics/ Newport (Santa Clara, California, USA)

G.2 LUMPlanFI/IR, 40x, 0.8 NA, water immersion objective, Olympus (Tokyo, Japan)

G.3 N16XLWD-PF, 16x, 0.8 NA, water-immersion objective, Nikon (Tokyo, Japan).

G.4 Emission filter 525/50 nm bandpass filter, AHF Analysetechnik (Tübingen, Germany)

G.5 Emission filter 607/70 nm, Chroma Technology (Bellows Falls, Vermont, USA)

G.6 Autocorrelator, Carpe, APE (Berlin, Germany)

G.7 Controller for Pockels cell, model 302RM, conoptics (Danbury, USA)

G.8 Data acquisition card, NI 6115, National Instruments (Austin, USA)

G.9 Data acquisition card, NI 6008, National Instruments (Austin, USA)

G.10 Dichroic mirror, 670 mm, Chroma Technology (Bellows Falls, Vermont, USA)

G.11 IR filter, type 092, 46 x 0.75, The Imaging Source Europe GmbH (Bremen, Germany)

G.12 Linear stage and motor, LTA-HS and M-UMR8.51, Newport (Santa Clara, California, USA)

G.13 Linear stage, M-VP-25-XA, Newport (Santa Clara, California, USA)

G.14 Low-noise current amplifier, SR570, Stanford Research Systems (Sunnyvale, California, USA)

G.15 Mirrors, E03, Thorlabs GmbH (Dachau, Germany)

G.16 Motion controller, ESP300, Newport (Santa Clara, California, USA)

G.17 Mounting material, Thorlabs GmbH (Dachau, Germany)

G.18 Photomultiplier tube, R6357, Hamamatsu (Toyooka, Japan)

G.18 Pockels cell, model 350-80, Conoptics (Danbury, Connecticut, USA)

G.20 Power supply, NMC-100, Conrad Electronic SE (Hirschau, Germany)

G.21 Resonant optical scanner, 12 KHz CRS, Cambridge Technology (Lexington, Massachusetts, USA)

G.22 Scan lens, 50 mm, Leica Microsystems GmbH (Wetzlar, Germany)

G.23 Tube lens, 300 mm, Thorlabs GmbH (Dachau, Germany)

G.24 Yanus scanhead, TILL Photonics GmbH (Martinsried, Germany)

G.25 FPTGA, NI PXIe-1073,National Instruments(Austin, USA)

2.2.9 Software

H.1 MATLAB, The MathWorks (Natick, Massachusetts, USA)

H.2 Psychosphysics Toolbox240, David H. Brainard, Department of Psychology, University of California (Santa Barbara, California, USA, http://psychtoolbox.org)

H.3 Colibri, a two-photon laser scanning microscope controlling software written in Lab- VIEW, LMU Biocenter and MPI of Neurobiology (Martinsried, Germany)

H.4 LabVIEW, National Instruments (Austin, Texas, USA)

3

Results

In this thesis, I investigated the effects of partial retinal lesions on the receptive field properties of V1 neurons in mice at the single-cell level using two-photon microscopy. Because of the known problems with first generation genetically-encoded calcium indicators such as GCaMP3 (Tian et al. [77], Zariwala et al. [84]) for long-term imaging, namely low signal to noise (SNR) and low number of responsive cells, I initially used a synthetic indicator, OGB1-AM. This approach has the severe disadvantage of not allowing repeated imaging of the same cells, but on the other hand has already been used in single cell receptive field mapping studies (Smith and Häusser [72], Bonin et al. [10]). While I was setting up the experiment in this manner, a new and much improved version of the genetically-encoded indicator GCaMP3 became available, GCaMP6s (Chen et al. [14]). Its larger signals and high SNR allowed detection of signals evoked by weaker stimuli and therefore permitted reliable receptive field detection. In combination with a structural marker (mRuby2) in a construct design by Tobias Rose (MPI of Neurobiology, Dept. Synapses-Circuits-Plasticity, Martinsried, Germany), this indicator became the method of choice for this study.

3.1 Protocol for assessing plasticity following retinal lesions

3.1.1 Imaging Calcium responses using OGB1-AM

Following loading of neurons with OGB1-AM (see chapter 2) I initially used full-field square wave moving gratings, a strong stimulus for V1 neurons, thereby allowing testing effective dye-loading and condition of the preparation. Next, I mapped receptive fields using a stimulation protocol very similar to that used for optic imaging of intrinsic signals (OI).

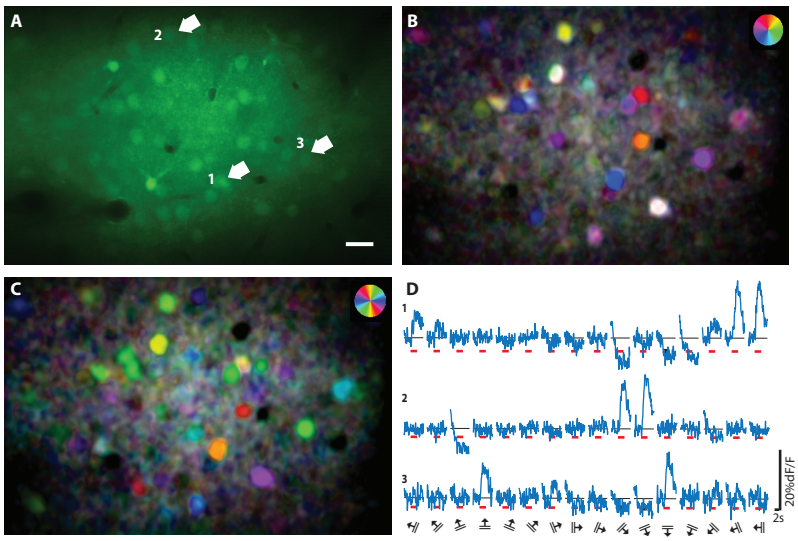

Figure 3.1.1 – Orientation and direction tuning measured with OGB1-AM (A) Optical section at 200µm depth labeled with OGB1-AM (green) Scale bar 20µm. White arrows indicate neurons for which time courses are shown in (D). (B) Pixel-based direction map with coding for preferred direction (hue), response amplitude (lightness) and tuning width (saturation). (C) Pixel-based orientation map with coding for preferred orientation (hue), response amplitude (lightness) and tuning width (saturation). (D) Average dF/F time courses of three representative neurons during stimulus presentation. Stimulus orientation and direction are indicated by symbols below. Red bar indicates duration of visual stimulation. (B,C) Orientation/direction preferrence color-coded in accordance with the pie chart on the top right of each map.

Panels B and C of figure 3.1.1 represent orientation and direction HLS maps which constitute a first approach to examine neuron responses to a given visual stimulus. Panel D shows tuning properties of OGB1-AM loaded cells in monocular V1. The average traces shown are representative examples of direction and/or orientation selective cells. As can be observed in the HLS maps, OGB1-AM allows for reliable mapping of orientation and direction selectivity of numerous cells at the same time.

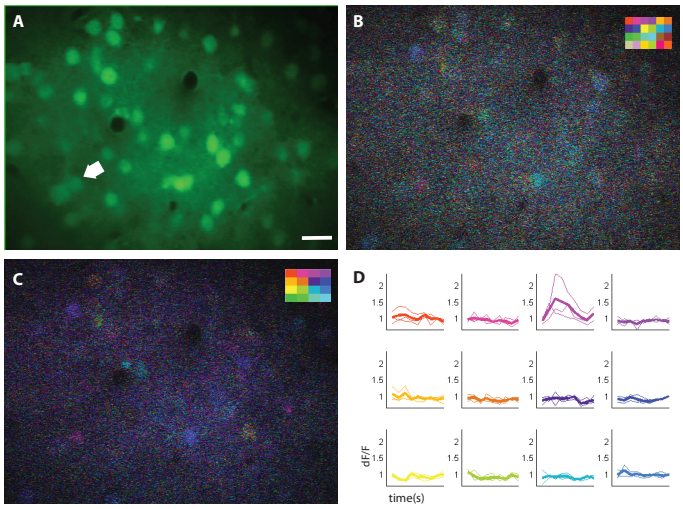

Figure 3.1.2 – Gross receptive field mapping with OGB1-AM (A) Optical section at 230µm depth labelled with OGB1-AM (green) Scale bar 15µm. White arrow indicates neuron for which individual time courses are shown in (D). (B) Pixel-based map of receptive field position mapped with a 6x4 visual stimulation grid (15° patch size). Identity and position of each stimulus is color-coded and shown in the right top corner. Color code indicates preferred stimulus position for each cell. (C) Pixel-based map of receptive field position mapped with a 4x4 visual stimulation grid (25° patch size). Identity and position of each stimulus is color-coded and shown in the right top corner. Color code indicates preferred stimulus position for each cell.(D) Single and average dF/F time courses for an example cell plotted over the mapped grid (4x4) in panel (C).

Figure 3.1.2 illustrates the results obtained when using OGB1-AM to map receptive fields using a stimulation paradigm analogous to the one I employed for OI, that is, discrete patches of moving gratings in alternating positions of the visual field. These stimuli are large (15°-25°) and therefore elicit big responses, and for this reason were chosen as a first step towards establishing the technique.

The polar maps shown here provide information about the preferred stimulus position as well as the signal strength. Panels B and C from Figure 3.1.2 show that the intensity and extent of the responses is lower than that elicited by full field moving gratings even though it is still possible to map gross receptive field position for around 30% of the cells in an imaging plane.

3.1.2 Imaging Calcium responses using GCaMP6s-mRuby2

As soon as the new genetically-encoded indicator GCaMP6s became available, I changed the approach and was therefore able to characterize the receptive fields of the same V1 neurons over time.

The properties of an example V1 neuron virally infected with the double construct mRuby2-GCaMP6s are depicted in figure 3.1.3. The structural marker mRuby2 (red) labels cells' nuclei, whereas the calcium indicator, GCaMP6s (green), is expressed in the cytoplasm,

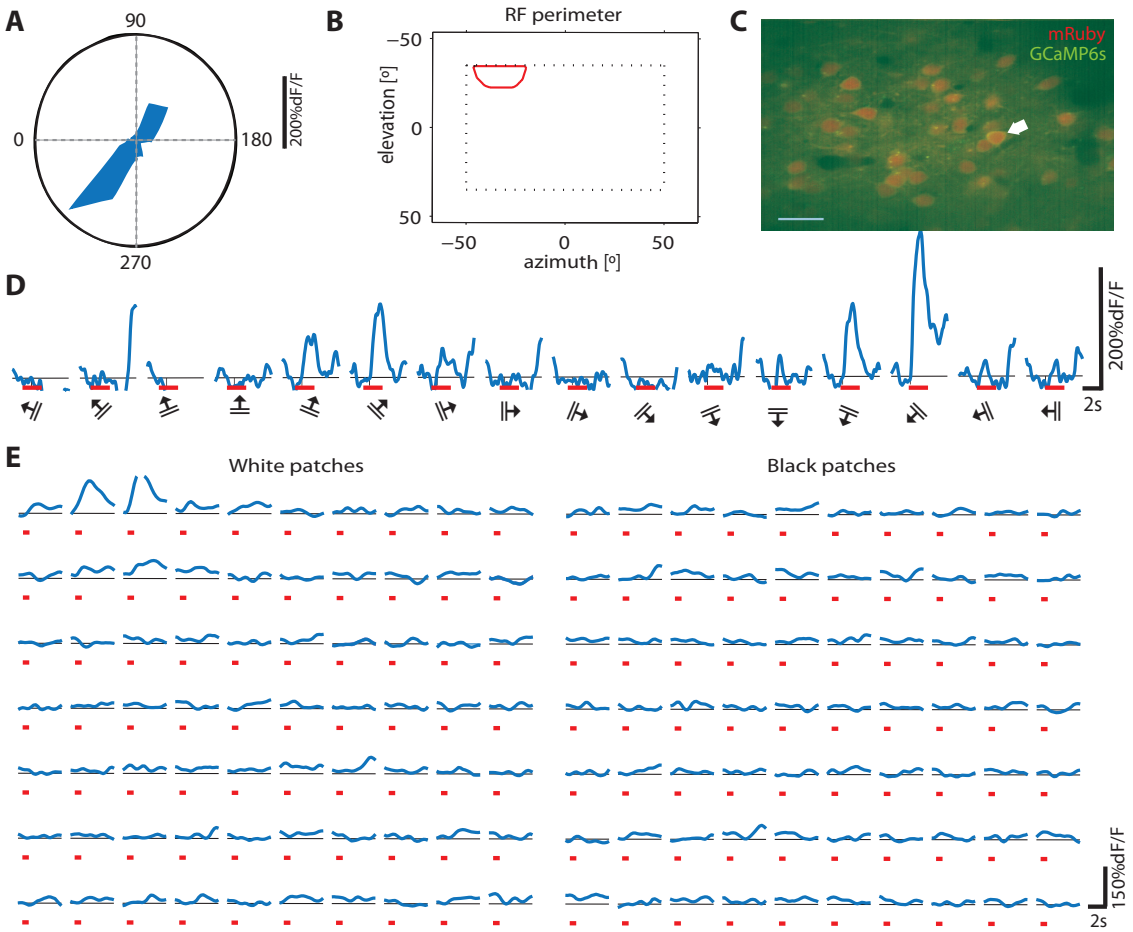

Figure 3.1.3 – RF characterization with GCaMP6s-mRuby (A) Polar plot of orientation tuning of an example cell labeled with GCaMP6s-mRuby. The cell is orientation and direction selective, with its preferred orientation around 315°. (B) Receptive field outline of the same cell (ON cell). The receptive field mapped is based on the responses to the visual stimuli shown in (E). Dashed line delimits the experimentally mapped area of visual field. (C) Overlay of structural and functional channels of a section of an imaging plane at 160µm depth. Red (mRuby), Green (GCaMP6s) Scale bar: 20µm. White arrow indicates example neuron. (D) Average dF/F time course for orientation tuning. Identity of stimulus (orientation and direction) indicated by symbols underneath. (E) Average dF/F time courses plotted over the mapped visual grid (10x7) for ON (white patches) and OFF (black patches) subfields. The location of the responses serves to determine size, position and type of the neuron's receptive field, in this case a single ON field. (D,E) Red bar indicates duration of stimulus.

as shown in panel C. Both, the orientation tuning (see panel A, representative polar plot and panel D, example dF/F time course for orientation tuning) and the receptive field structure, including ON and/or OFF subfields, could be determined very precisely with this approach, mainly due to the indicator´s improved sensitivity (see panels B: position of receptive field outline and panel E: example dF/F time courses at different positions of

visual space). Consequently, even small mapping stimuli (10°) could be used to acquire reliable data.

The stable expression levels of the double construct GCaMP6s-mRuby allowed for the chronic assessment of neurons' receptive field properties crucial for imaging long-term plasticity. The data shown in figure 3.1.4 provides an example of a monocular V1 neuron's receptive field map characterization at thirteen successive time points over a two month period. This cell corresponds to an imaging region located far away from the LPZ (more than 350µm away from its center) after retinal lesions.

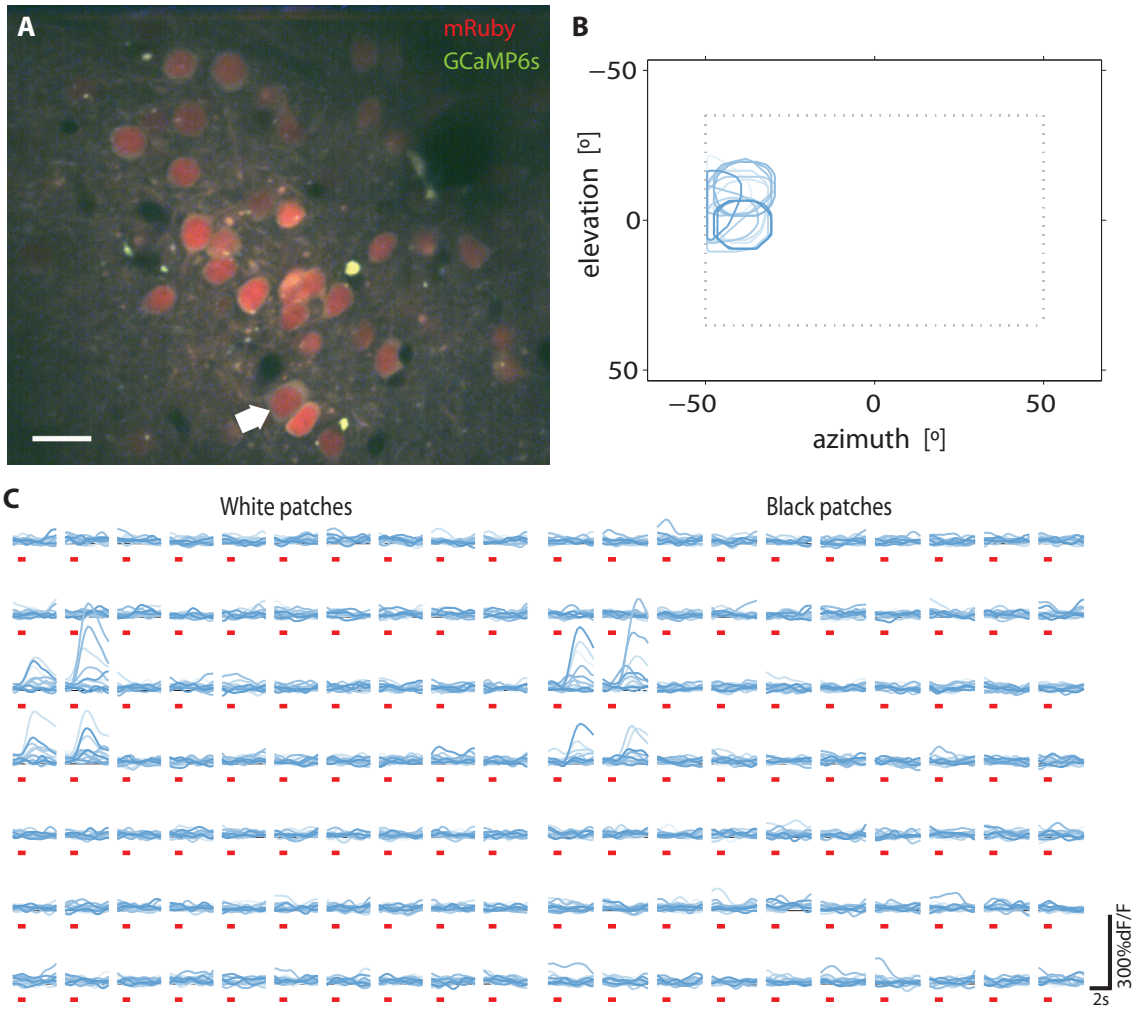

Figure 3.1.4 – **Chronic receptive field mapping with GCaMP6s-mRuby** (A) Overlay of structural and functional channels of a section of an imaging plane at 150µm depth. Red (mRuby), Green (GCaMP6s) Scale bar: 20µm. (B) Overlay of receptive field outlines of an example cell recorded over 13 imaging sessions. The receptive fields mapped is based on the responses to the visual stimuli shown in (C). Dashed line delimits the experimentally mapped area of visual field. (C) Average dF/F time courses for the same cell displayed over a stimulus grid (10x7) for ON (white patches) and OFF (black patches) subfields obtained in 13 subsequent imaging sessions. The location of the responses serves to determine size, position and type of the neuron's receptive field. Note the offset responses to the black patches, consistent with the onset responses to the white patches at the same spatial positions, this cell had a single ON field in all recordings. (B), (C) Darker blue shading corresponds to later imaging time points.

3.2 Analysis of plasticity after retinal lesions

For this study on single-cell plasticity four mice underwent small retinal lesions in the eye contralateral to the hemisphere where the genetically-encoded calcium indicator

GCaMP6s-mRuby was expressed. These animals were imaged both with optical imaging of intrinsic signals to determine the overall retinotopic map and the location of the LPZ, and with 2-photon microscopy to record single-cell activity at the intervals shown in figure over a two month period.

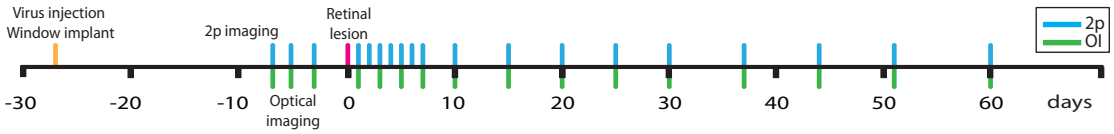

Figure 3.2.1 – **Experimental timeline** Description of the experimental setup for this study on plasticity after RL. Three weeks prior to RL, the virus expressing the calcium indicator was injected and an imaging window implanted. Two weeks after, when expression was sufficient for imaging, animals underwent one to three baseline 2p-imaging sessions. Subsequently, a small retinal lesion was made in one eye and afterwards animals were imaged daily for the first week, once every five days until a month after RL, and weekly for the second month . The optical imaging regime was basically identical to the 2p-imaging except for the first week after RL, where animals were imaged once every two days. OI: optical imaging; 2p: 2photon-imaging

3.2.1 Extent of retinal lesions

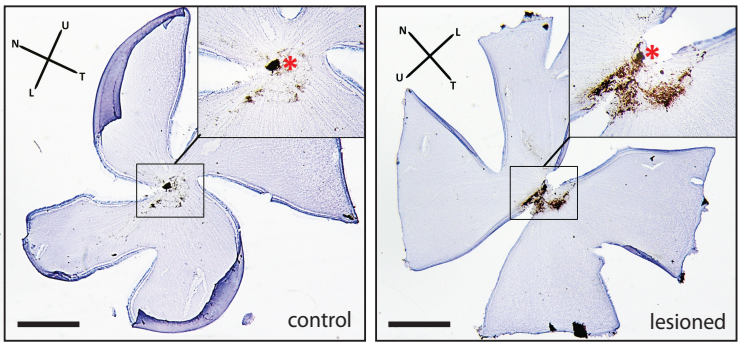

Figure 3.2.2 – **Extent of retinal lesions** Cresyl-violet stained retinas from control (left) and lesioned eye (right). Damage to the retina as a result of laser photocoagulation is shown by the scar tissue in the dorso-temporal side around the optic disc. Scale bar: 500µm. Retinal axes: L: lower; N:nasal;T;temporal; U:upper/dorsal. Asterisk (*) marks approximate position of the optic disc.

To assess the extent of the retinal lesion caused by laser photo-coagulation and to confirm its location, retinas were stained with cresyl-violet which confirmed the position of the lesion: dorso-temporal and above the optic disc. Its average size was 400µm in the vertical axis and 550µm in the horizontal axis, slightly smaller than the values reported in Keck et al. [47] and corresponding to ~20° along the horizontal meridian in visual space.

3.2.2 Progression of functional recovery after RL as determined with OI

Characterizing the changes in the deprived cortical region after a lesion with OI was important, since it permitted not only the localization of the LPZ and the relative position of the 2-photon imaging regions with respect to it, but also helped to assess the overall progression of recovery. Figure 3.2.3 shows the color coded retinotopic maps obtained for one mouse before and at different time points after the lesion. The extent of the initial lesion projection zone (LPZ) and different steps of the recovery can be readily observed in these maps.

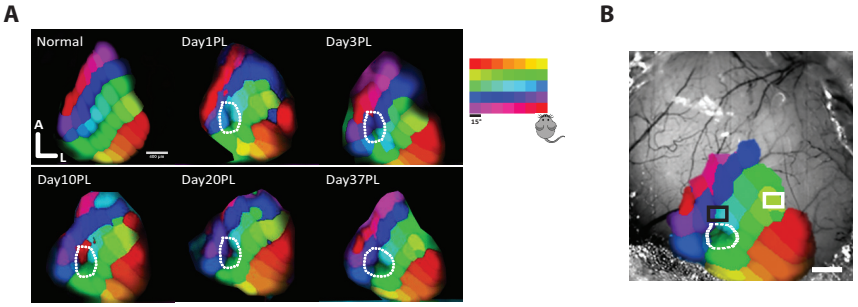

Figure 3.2.3 – Retinotopic maps before and after RL and imaging locations relative to LPZ (A) Retinotopic maps of one mouse before and at different time points after retinal lesion. Distortion in the maps seems to decrease over time even though more than a month after retinal lesion the "filling-in" is not yet complete. Top right: color coded layout of stimuli. Patch size: 15°; A: anterior; L: lateral. PL: post lesion. (B) Overlay of retinotopic map and bloodvessel pattern image showing 2p-imaging regions. Black square: region close to the LPZ (close). White square: region far from LPZ (far). White dashed line: LPZ outline. Scale bar: 400µm.

As mentioned above, these data provided the basis for the identification of the relative positions of the imaging regions for the chronic single-cell imaging. In figure 3.2.3 two 2-photon imaging regions were overlaid over the functional map of an experimental mouse one day after retinal lesions and displayed over the blood vessel pattern image for reference. These regions exemplify the two sets of data analyzed in this study: the first comprises regions far away from the LPZ (far), defined as being located more than 350µm away from the center of the LPZ (4 mice, 4 imaging planes, 60 cells) and the second covering those in the vicinity of the LPZ (close), 100µm-200µm away (4 mice, 6 imaging planes, 70 cells).

3.2.3 Retinal lesions decrease stimulus-driven activity levels in cells close to the LPZ

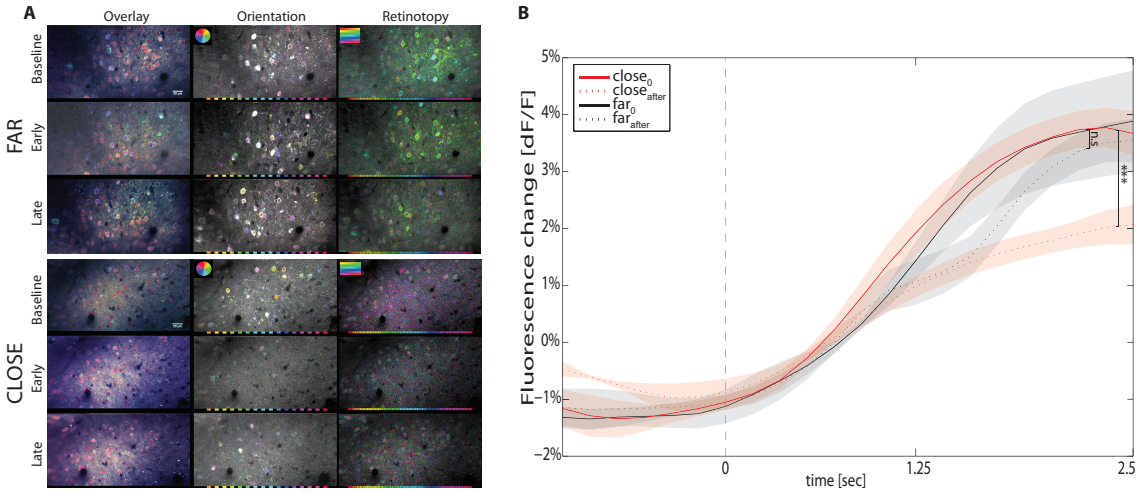

Figure 3.2.4 – Visually-driven activity levels drop significantly after RL in regions close to the LPZ (A) Comparison of activity levels in far vs close to LPZ regions, reflected in HLS maps for orientation tuning and RF preference at two time points after RL (early: 2 days after, late: 30 days after). In regions close to the LPZ in both HLS maps there is a clear decrease in the number of colored cells after retinal lesion, especially when compared to the region far from the LPZ where there appears to be barely any change in the number of colored cells in both types of maps after retinal lesion. HLS: preferred orientation/preferred stimulus position (hue), response amplitude (lightness) and tuning width (saturation). Scale bar: 200µm. Overlay: image combination of structural channel (mRuby) and activity channel (GCaMP6s). The color code for the orientation plots marks orientation preferrence whereas in the retinotopy plots the color shading corresponds to the location in the visual field marked by the position of the stimulus over the color-coded grid. (B) Average dF/F time courses for all cells in close/far regions during visual stimulation before and after retinal lesion. There is a highly significant decrease in visually-evoked activity after retinal lesion in regions close to the LPZ whereas those far from it barely change. Dashed vertical line represents stimulus onset. All traces represent mean±SEM. (***) p<0.001, (n.s) not significant, Wilcoxon sign-rank test.

Removal of direct afferent drive is expected to reduce visual drive, thus I assessed stimulus-evoked activity levels after RL. To that end I averaged the responses for all cells in three far regions versus three close regions (200 cells in total for close and/or far, 3 mice) for all periods of visual stimulation with full field gratings.

I performed this kind of analysis before as well as after RL. The traces of all time points after RL were averaged to estimate the overall change in stimulus-driven activity levels after RL.

Figure 3.2.4 depicts the difference in the visually-evoked response amplitudes for neurons in regions close to and far from the LPZ after RL. Close to the LPZ the decrease is large and significant, while in regions far from it there is no difference to baseline levels.

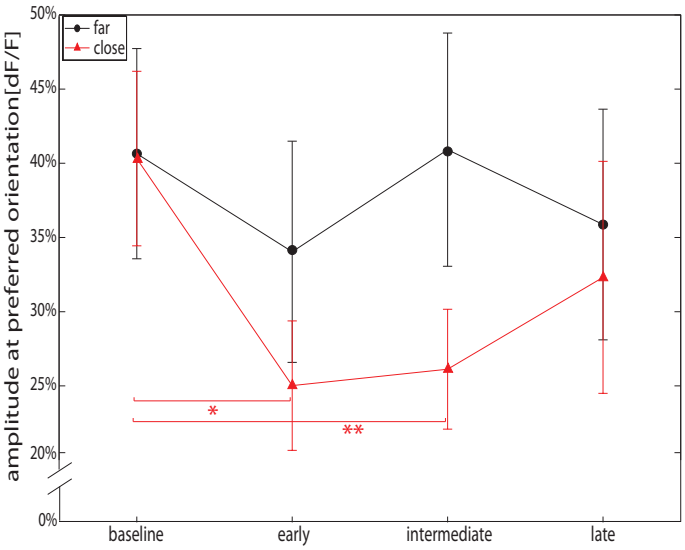

Figure 3.2.5 – Amplitude at preferred orientation is significantly decreased after RL in regions close to the LPZ Peak amplitude at preferred orientation before and after retinal lesion barely changes for cells far from the LPZ whereas in cells close to it during the first month after the retinal lesion there is a significant decrease in amplitude that at later time points tends to revert to baseline levels but still remains lower than those. Error bars: SEM, (within region test: (*)p<0.05; (**) p<0.005; Wilcoxon sign-rank test with Bonferroni correction; among regions test: n.s. U-Mann Whitney test with Bonferroni correction)

Given the significant decrease in overall visually-driven activity in regions close to the LPZ, I tested whether the mean amplitude at the preferred orientation (PrefOri) also changed for cells in this region and found that, in agreement with those results, there is a significant decrease (Wilcoxon sign-rank test with Bonferroni correction for multiple comparisons) in the mean amplitude of the responses at preferred orientation at the early and intermediate time-bins. This decrease is maintained even at the late imaging time points for cells close to the LPZ, even when there is a tendency towards normalization. In contrast, variations to the amplitude for cells far from it are of a much smaller scale and not significant. Despite these differences, the mean amplitudes for cells close and far from the LPZ at each time-bin are not significantly different (U-Mann Whitney test with Bonferroni correction).

3.2.4 Retinal lesions decrease receptive field detection rates in regions close to the LPZ

Changes to receptive field position and size are a well-known effect of retinal lesions, therefore I set to determine the aforementioned receptive field properties for neurons belonging to each of the two spatially defined data sets previously mentioned, far and close, at each of the imaging time points indicated in figure 3.2.1.

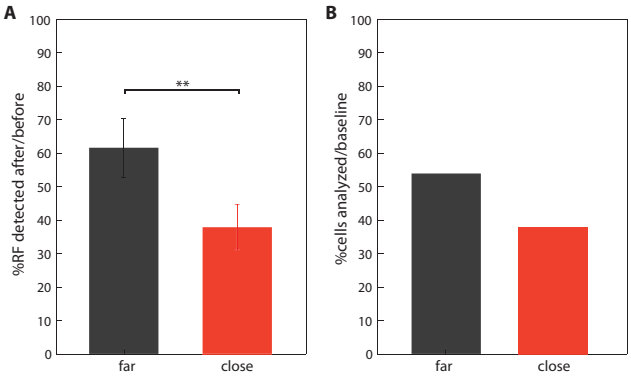

Figure 3.2.6 – Receptive field detection accuracy decreases after RL in regions close to the LPZ (A) Percentage of cells for which an accurate receptive field could be detected after retinal lesions normalized to the average number of cells with a RF detected at baseline. Nearly 20% more cells had an accurate receptive field detected after retinal lesion in regions far from the LPZ than close to it. Error bars: SEM. (**) p<0.005; U-Mann Whitney test (B) Percentage of cells for which an accurate RF could be detected in at least 4 time points aside from a baseline time point (far: 4 mice, 6 imaging planes, 70 cells; close: 4 mice, 4 imaging planes, 60 cells) normalized to the total number of cells with a RF detected at baseline (far: 4 mice, 6 imaging planes, 130 cells; close: 4 mice, 4 imaging planes, 158 cells). More than 15% more cells were included in the far dataset than in the close dataset of all cells with a RF detected at baseline.

I found that after retinal lesions accurate detection of receptive fields decreased significantly more for cells located close to the LPZ than for those far from it ($p<0.005$; U-Mann Whitney test). Figure 3.2.6 panel A shows that the proportion of receptive fields detected after retinal lesions drops to about 40% of those measured at baseline for cells close to the LPZ whereas for those far from it the proportion lies around 60%.

For the longitudinal analysis of functional plasticity after retinal lesions I applied a selection criterion based on receptive field detection. Only cells for which a receptive field could be accurately detected at baseline and at least four other time points after retinal lesions were included in the dataset (130 cells, 4 mice, 10 regions). Panel B in figure 3.2.6 depicts the proportion of cells included in the analysis with respect to the total number of cells for which a receptive field was detected at baseline for each subset (close and far). More than 50% of the initial pool of neurons with an accurate receptive field were used for fur-

ther analysis in the case of cells located far from the LPZ whereas for those close to it the percentage dropped below 40%.

Nearly 60% of all cells included in the analysis (both in far and close regions) had a single ON field; the remaining 40% had a single OFF field, therefore cells were classified according to their receptive field type for all analyses. Three different time bins were defined after retinal lesions corresponding to different stages of the recovery period: early (day1-day10 post-lesion), intermediate (day15-day30 post-lesion) and late (day37-day65 post-lesion). Data in each of these time bins' corresponds to an average of all time-points belonging to it.

3.2.5 Retinal lesions alter receptive field position and size

A hallmark of retinal lesion studies is the finding of receptive field shifts (Kaas et al. [45], Gilbert et al. [26], Gilbert [25], Gilbert and Wiesel [30], Giannikopoulos and Eysel [24], Abe et al. [1]). I therefore determined the RL-related relative shifts of the receptive field for neurons located both far and close to the LPZ.

The average jitter of receptive field position at baseline was small: 3.45°±0.33 for cells far from the LPZ and 4.88°±1.31 for cells close to it (n.s.,Mann Whitney U-test, 20 cells).

However, both ON and OFF cells located close to the LPZ (60 cells, 4 mice, 6 regions) showed a significantly (Mann Whitney U-test) higher average RF shift from baseline position than those far (70 cells, 4 mice, 4 regions) away from it at all time-bins considered, except OFF cells at the late time-bin (figure 3.2.7). Panel C of figure 3.2.7 shows individual examples of receptive field displacement at the different time bins for 4 cells far from the LPZ and 5 located close to it. As can be observed, there is a bigger spread of receptive field shifts in cells located close to the LPZ and the magnitude of the shifts is generally larger than for cells far from the LPZ.

Receptive fields have been described to shift outwards from the LPZ (Kaas et al. [45], Gilbert et al. [26], Gilbert [25], Gilbert and Wiesel [30], Giannikopoulos and Eysel [24], Abe et al. [1]), therefore I determined the direction of the receptive field shifts found in

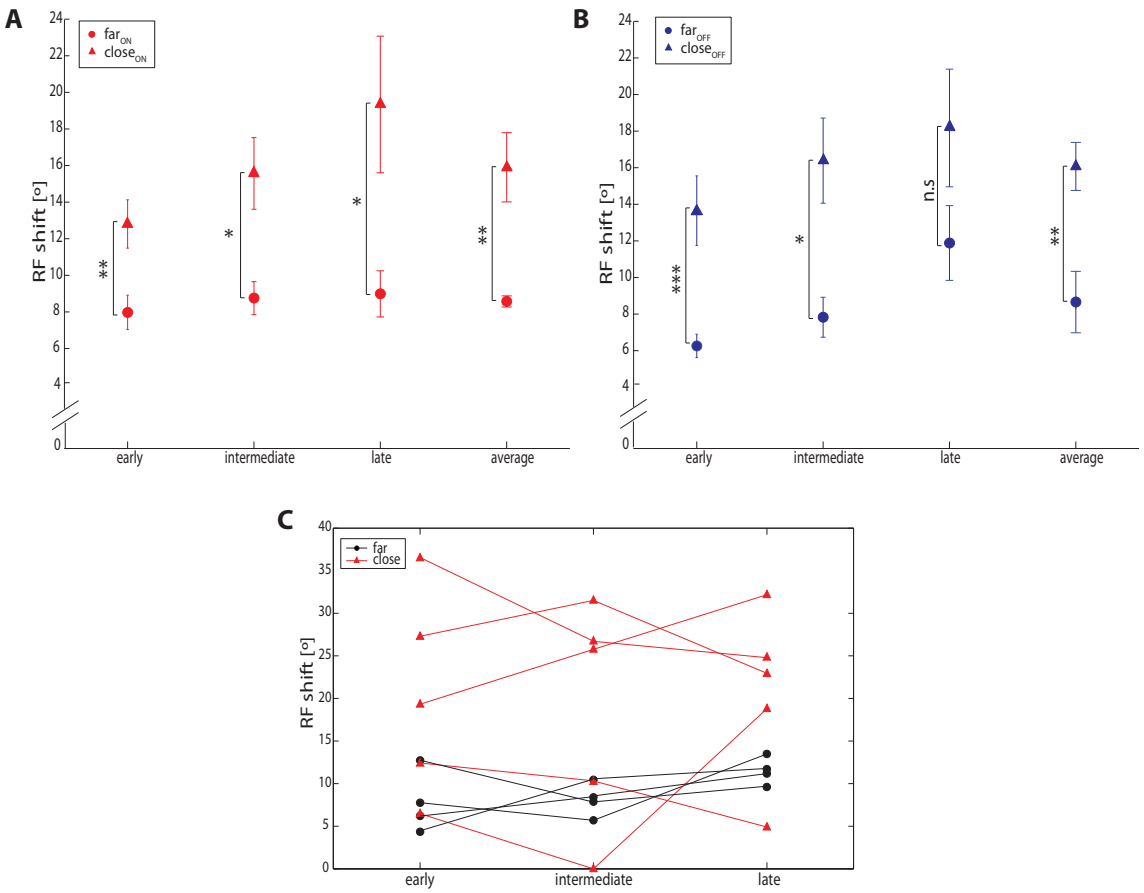

Figure 3.2.7 – RF close to LPZ shift more than those far from it (A) Average (mean±SEM) RF center displacement for ON cells. ON receptive fields of cells close to the LPZ show significantly larger shifts than those far from it at all time bins tested. (B) Average (mean±SEM) RF center displacement for OFF cells. OFF receptive fields of cells close to the LPZ show significantly larger shifts than those far from it during the first month after retinal lesion. (C) RF shifts for single cells from regions far (4 cells) and close (5 cells) to the LPZ at each time bin. Receptive field shifts of cells close to the LPZ are much more variable and of greater magnitude than those of cells far from it. (*)p<0.05; (**) p<0.005; (***) p<0.001, (n.s) not significant, U-Mann Whitney Test.

this study. Plotting a direction vector from the initial RF center position to its average location (geometric median) after the lesion in the regions close to the LPZ from all four experimental mice shows a clear diversity of receptive field changes, not only in distance from the original position but also in the direction of the shift (see figure 3.2.8). Careful observation, however, allows to discern a certain pattern in the shift of a majority of cells in each region tested. To characterize this pattern I performed a vector analysis over each of these regions alone and found that there is a tendency for cells, on average, to shift their RF centers away from the LPZ (see figure 3.2.8). For each of those regions,

the calculated average vector for all receptive fields in each of the regions tested pointed away from the LPZ. For illustration of the effect, examine average receptive field center position with respect to the LPZ in figure 3.2.8 left panels and observe the direction of the corresponding average vector in figure 3.2.8 right panels.

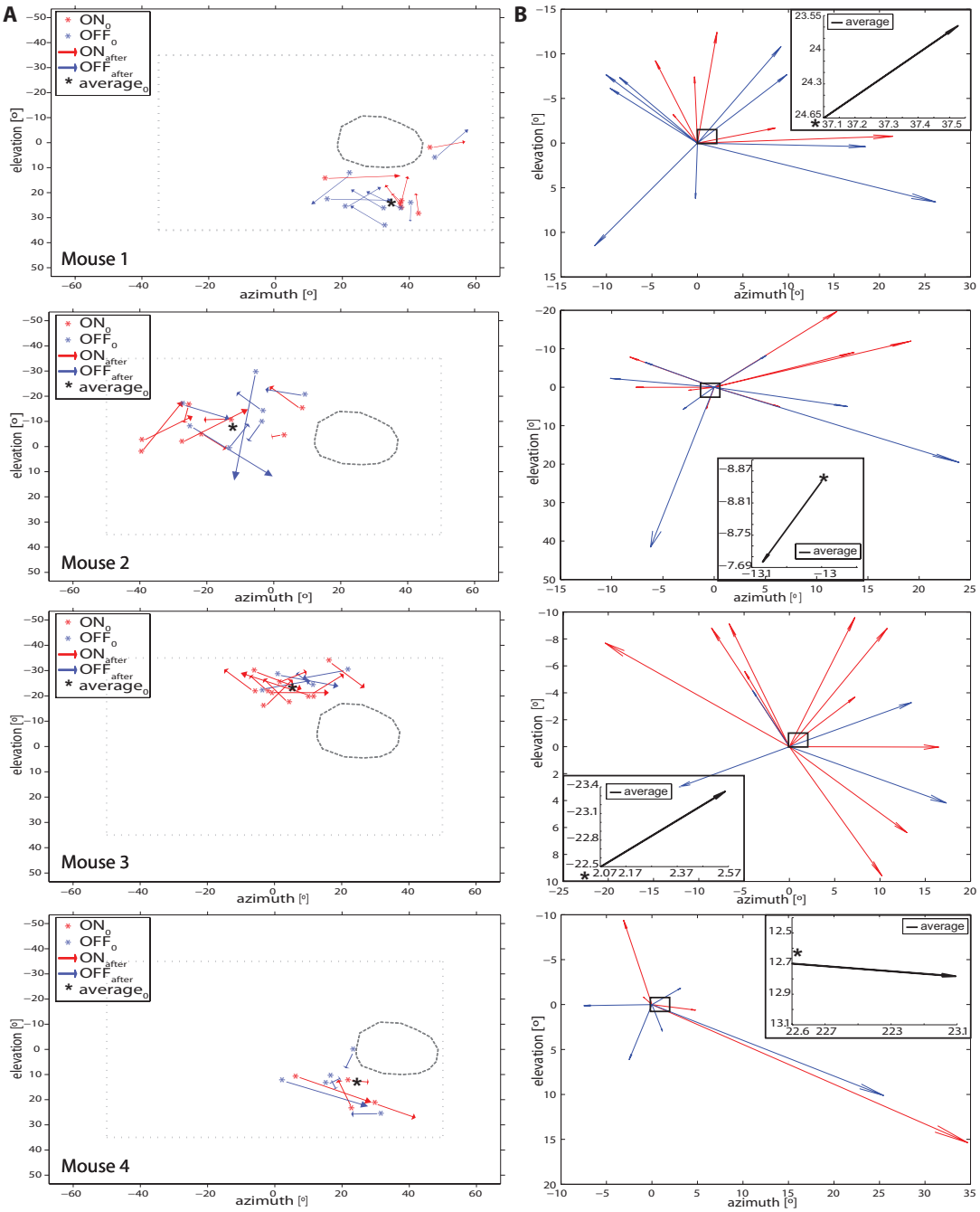

Figure 3.2.8 – Receptive fields shift away from the LPZ in regions close to LPZ (A) Each plot corresponds to a region close to the LPZ in four different mice. Red: ON fields; Blue: OFF fields. Vector size and direction illustrate mean receptive field shift after retinal lesion for each cell. Dashed outline marks LPZ contour. Black asterisk marks average baseline position for all receptive field centers (ON&OFF). There is a great variability in the size and direction of the shift of receptive fields for each animal/region but an overall pattern can be discerned in the shift. (B) Plots on the right show all direction vectors used for vector analysis and shifted to the same origin (0,0). Insets show the average vector for all receptive field shift vectors with the axes centered at the average baseline RF center position for each region. Taking the average position of all receptive field centers before RL and the average vector of all receptive field shift vectors, it shows that in general the average vectors in all cases point away from the LPZ.

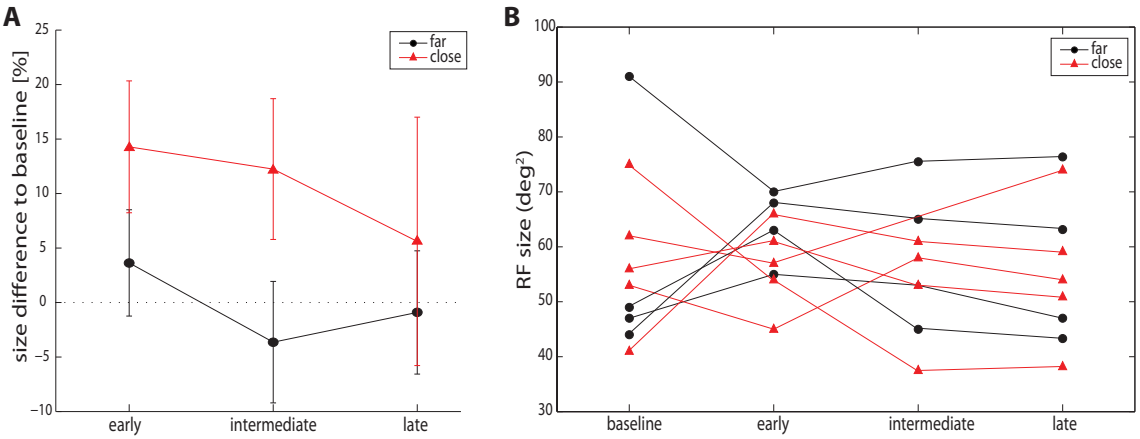

Figure 3.2.9 – Receptive field size changes after retinal lesions (A) Relative change in size in respect to baseline. Error bars: SEM, (within region test: n.s. Wilcoxon sign-rank test with Bonferroni correction; among regions test: n.s. U-Mann Whitney test with Bonferroni correction). Receptive field size of cells close to the LPZ increases after retinal lesions, however this increase tends to revert back to baseline at late time points, even when they remain larger than at baseline. (B) Receptive field size of single cells from regions far (4 cells) and close (5 cells) to the LPZ at each time bin. Receptive field size is very variable, even at baseline, and this variability is maintained after retinal lesions both for cells close and far from the LPZ.

I also evaluated RL effects on receptive field size, another property that has been previously described to change after RL in cats (Giannikopoulos and Eysel [24]). I found that, for receptive fields (ON and OFF fields were analyzed together) located either in close (average size (deg^2) at baseline: 49±1.7; early: 56±1.2; intermediate: 55±1.6; late: 51.±2.7) or far (average size (deg^2) at baseline: 55±1.6; early: 57±0.9; intermediate: 53±1.8; late: 54.5±2.4) away regions from the LPZ there is a trend towards an increasing average size (deg^2) during the early phase of the recovery after the lesion. This effect tends to decrease and size returns back to baseline size in regions far from the LPZ whereas, in regions close to it, it does not decrease to baseline levels. In figure 3.2.9 panel A the relative changes in RF size to baseline at each time-bin are plotted for comparison between regions close and far from the LPZ. Panel B shows receptive field size for individual cells located close and far from the LPZ before and after retinal lesions at all time bins. Receptive field sizes are very variable even for cells from the same region, and this variability, which is observed already at baseline, persists after retinal lesions.

Figure 3.2.10 shows one example cell each from a region close and a region far from the

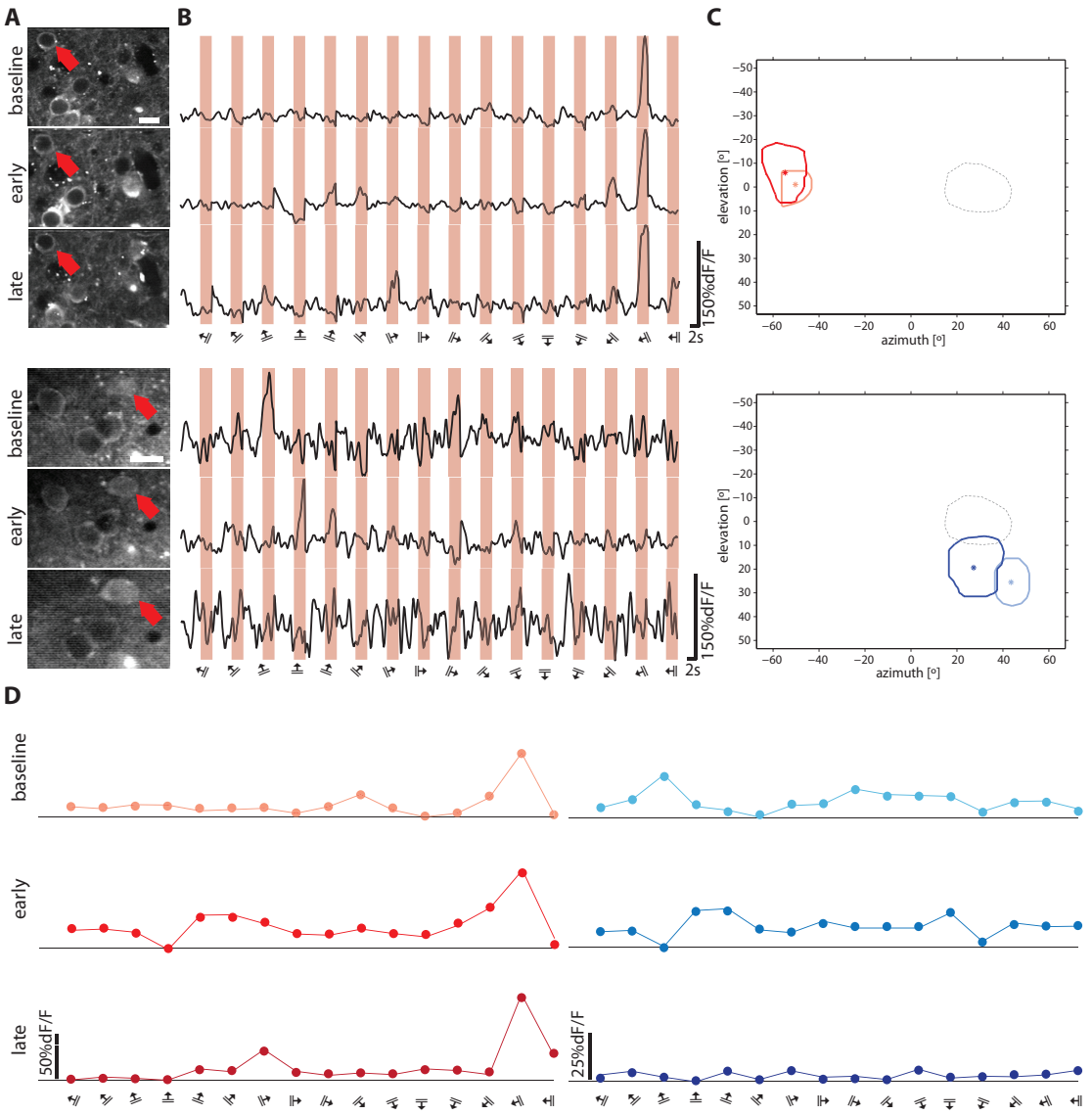

Figure 3.2.10 – Example showing differences in the effects of a retinal lesion on cells close and far from the LPZ (A) Same cell depicted at different time-points in the activity channel (GCaMP6s). Top: cell far from the LPZ; Bottom: cell close to the LPZ. Red arrow points to the example cells. Time points: baseline; early (2 days after retinal lesion); late (37 days after retinal lesion). Scale bar: 10µm (B) dF/F response curves to full-field moving gratings. Shading indicates presence of stimulus. Identity of stimulus (orientation and direction) indicated by symbols underneath. (C) Location of RF centers and perimeters before and after (geometric median) retinal lesion. Dashed line: LPZ outline. Dark color represent location of receptive field after retinal lesion. Top: cell far from the LPZ; Bottom: cell close to the LPZ. Note the difference in the degree of the shift in the position of the receptive fields before and after for both cells. (D) Orientation tuning curves corresponding to the transients in (B). Identity of stimulus (orientation and direction) indicated by symbols underneath. Red colormap: cell located far from the LPZ; Blue colormap: cell close to the LPZ. While the cell located far from the LPZ maintains its tuning after retinal lesion, the cell close to the LPZ first shifts its preference and in the end loses orientation tuning altogether.

LPZ (panel A), their raw average calcium traces at baseline, early (2 days after RL) and late (37 days after RL) in panel B, as well their respective receptive fields at baseline and their average position and perimeter after RL in panel C. The example from the region far from the LPZ maintains its tuning throughout the experiment but the one close to it first shifts its orientation tuning curve and then loses tuning altogether, an effect that can be better appreciated from the tuning curves in panel D. The effects on receptive field size and position are representative of what was found for each of those regions on average, with greater changes in RF position and size in the example cell close to the LPZ.

3.2.6 Orientation tuning is not significantly altered after retinal lesions

One important property of V1 neurons is orientation tuning. To determine the influence of RL on neurons' orientation tuning in regions far or close to the LPZ, I made use of the same dataset as in section 3.2.5 and used the same time-bins for analysis. First, to characterize the stability of orientation selectivity after retinal lesions, I defined five categories based on the maintenance of this property, which is defined by having an OSI>0.5.

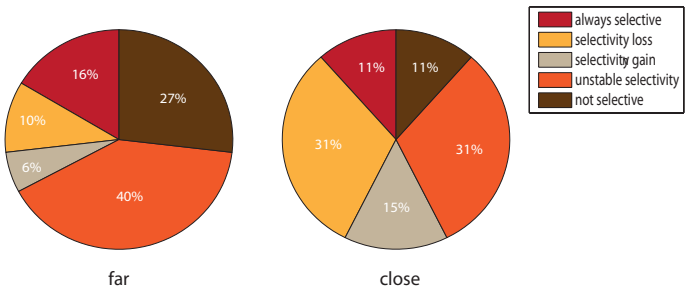

Figure 3.2.11 – **Stability of orientation selectivity.** Cells close to the LPZ show a bigger variability in orientation selectivity as shown by the proportion of cells that gain, lose or are unstably orientation selective.

Always selective: cells that remained orientation selective throughout the whole experiment (baseline plus the three time-bins after RL); *Selectivity loss*: cells that lost their orientation selectivity at any time-bin after the RL and never recovered it; *Selectivity gain*: cells not selective at baseline that became selective after the RL and maintained it un-

til the end; *Unselective cells*: those that were never orientation selective and *Unstable selectivity*: the remaining cells, not belonging to any of the aforementioned categories, being selective at some timebins but not at others without a discernible pattern.

I found that for cells located close to the LPZ, the proportions of always selective and never selective were equal and small (11% of the total), whereas most of the cells either lost their orientation selectivity (31%) or were unstable (31%). The remaining 15% of cells gained orientation selectivity after RL. In regions far away from the LPZ, the proportion of cells that maintained their orientation selectivity was slightly larger (16%), although there were more unselective (27%) and unstable cells (40%). However, fewer cells lost (10%) or gained (6%) orientation selectivity. Overall, it appears that cells located close to the LPZ are less stable than those far away from it, since the sum of cells losing, gaining or unstably shifting their orientation selectivity is larger in this region (close: 77%; far: 56%).

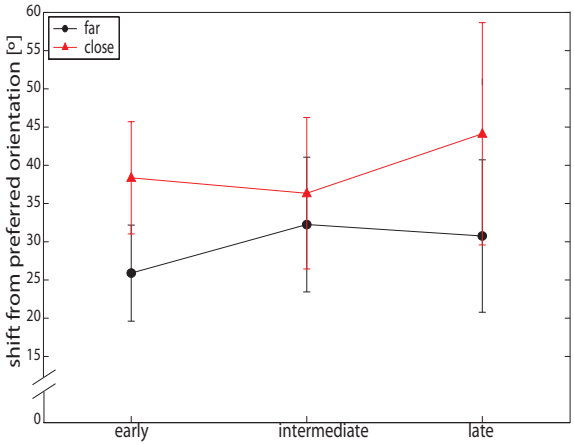

Figure 3.2.12 – Retinal lesions do not significantly affect preferred orientation The shifts from preferred orientation for cells located either far or close to the LPZ do not change significantly over time, neither do they differ depending on their location with respect to the LPZ. Error bars: SEM, (within region test: n.s. Wilcoxon sign-rank test with Bonferroni correction; among regions test: n.s. U-Mann Whitney test with Bonferroni correction)

Despite these differences, the average OSI for cells located close to the LPZ (60 cells, average OSI at baseline: 0.86±0.04; early: 0.89±0.02; intermediate: 0.79±0.05 and late: 0.79±0.06) did not differ much from that of cells far from it (70 cells, average OSI at baseline: 0.85±0.05; early: 0.83±0.04; intermediate: 0.87±0.04 and late: 0.67±0.08).

To assess more subtle lesion induced changes, I limited the analysis to the subset of cells that were orientation selective (OSI>0.5) at baseline (*always selective, selectivity loss, and selected cells from the unstable cell group*) and then determined the variation in preferred orientation (PrefOri) and preferred direction (PrefDir) from baseline and

bandwidth (BW).

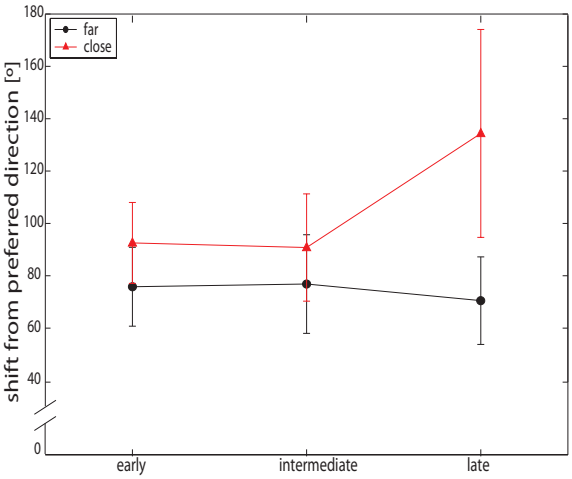

Figure 3.2.13 – No significant shift from preferred direction can be observed after retinal lesions The shifts from preferred direction for cells located either far or close to the LPZ do not change significantly over time, neither do they differ depending on their location with respect to the LPZ. Error bars: SEM, (within region test: n.s. Wilcoxon sign-rank test with Bonferroni correction; among regions test: n.s. U-Mann Whitney test with Bonferroni correction)

Figure 3.2.12 depicts the average size of shifts from baseline preferred orientation for cells in far and close regions at the three time-bins after lesion. Cells in regions close to the LPZ (35 cells, 4 animals, 6 regions) do not show a significantly different (U-Mann Whitney test with Bonferroni correction) absolute shift of preferred orientation than those far (29 cells, 4 mice, 4 regions) from it at all time-bins tested. Overall, neither cells close nor far from the LPZ change their average shift from preferred orientation significantly over time (Wilcoxon sign-rank test with Bonferroni correction for multiple comparisons).

Similarly to changes to preferred orientation, when I examined the shift from the preferred direction, I found no significant difference in the magnitude of the shift from preferred direction between cells located far and close to the LPZ (n.s., U-Mann Whitney test with Bonferroni correction), neither do they shift their preferred direction significantly over time (Wilcoxon sign-rank test with Bonferroni correction for multiple comparisons).

After retinal lesions, tuning width of cells close to the LPZ does not significantly (Wilcoxon sign-rank test with Bonferroni correction for multiple comparisons) change with respect to baseline, however there is a trend towards narrowing, as depicted in figure 3.2.14. Neither changes for neurons far from the LPZ which only tend to increase their bandwidth in the latest time-bins (Wilcoxon sign-rank test with Bonferroni correction for multiple comparisons). No significant differences were detected either between the two regions at any of the time-bins tested (U-Mann Whitney test with Bonferroni correction).

3.2.7 Summary: effects of retinal lesions on visual cortex plasticity

After successfully determining the extent and location of the retinal lesions and assessing the location of the LPZ with optical imaging of intrinsic signals (OI), I could reproduce the results of Keck et al. [47], which show an almost complete functional recovery in mouse V1 after retinal lesions with OI. Subsequently, 2-photon imaging experiments led me to the description of RL-related changes to receptive field and tuning properties of cells located in two distinct cortical regions according to their relative distance to the LPZ: close and far.

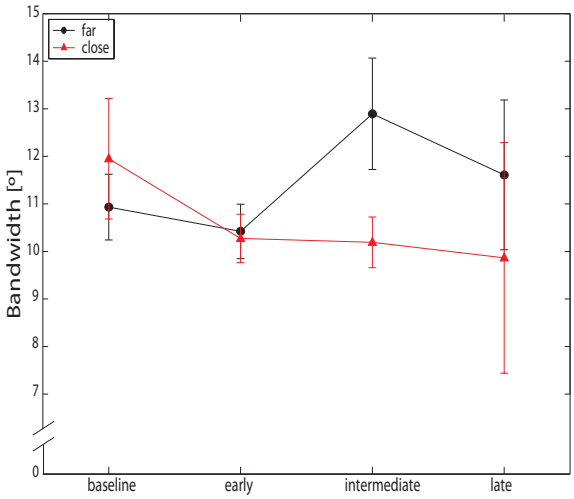

Figure 3.2.14 – Bandwidth does not significantly change in cells close or far from the LPZ after RL Bandwidth tends to decrease after retinal lesions in cells close to the LPZ, whereas this tendency is inverted in cells far from the LPZ two weeks after retinal lesions. However, theses changes are not significant. Nor are the differences between cells close and far from the LPZ at any time bin. Error bars: SEM, (within region test: n.s. Wilcoxon sign-rank test with Bonferroni correction; among regions test: n.s. U-Mann Whitney test with Bonferroni correction)

First, I found a significant decrease in visually evoked activity in cells close to the LPZ after retinal lesions, in agreement with the finding of a significantly decreased response amplitude at preferred orientation for cells close to the LPZ during the first month after retinal lesions. Next I could show that receptive fields shift from their original position to a significantly greater degree for cells located close to the LPZ than for those far from it, and that the average direction of this shift points away from the LPZ position. Also, I detected dynamic changes in receptive field size that correlate with the progression of the functional recovery, namely an early increase in receptive field size in cells in both regions that tends to return back to baseline at later time bins after retinal lesions.

Orientation and direction tuning are moderately affected by retinal lesions as evidenced by the fact that both cells far and close to the LPZ experience only subtle changes in their orientation selectivity after retinal lesions, (see figure 3.2.11) and, when cells maintained

their orientation selectivity, their preferred orientation, preferred direction and bandwidth do not significantly change, independently of their location with respect to the LPZ.

4

Discussion

In this thesis I have used two-photon calcium imaging to characterize *in vivo* functional plasticity in mouse V1 in a retinal lesion model of adult plasticity with **single-cell resolution**. Retinal lesions have long been shown to produce structural and functional changes at the cortical level in a number of model systems (cats, monkeys, rats and mice). However, all these studies (Gilbert [25], Gilbert and Wiesel [30], Darian-Smith and Gilbert [16], Giannikopoulos and Eysel [24], Keck et al. [47], Palagina et al. [65]) lacked the spatial and temporal resolution that the combination of two-photon microscopy and calcium imaging used in this study provided.

In this study, I have followed the progression of functional recovery in the visual cortex after small retinal lesions for a period of up to two months. I have characterized the relevant neuronal properties (receptive field position and size, orientation and direction tuning) in a chronic manner for the same cells over a baseline period and after deprivation.

One of the goals of this study was to determine if any potential functional changes depended on a neuron's spatial distance from the LPZ. To address this question, I collected data from distinct cortical regions located either close to (100µm-200µm away) or far from the LPZ (more than 350µm away) and compared their functional properties.

First, I found a prolonged and significant decrease in visually-driven activity levels in regions close to the LPZ after retinal lesions that correlates with a significant reduction in peak amplitude at the preferred orientation.

Second, receptive fields of cells located close to the LPZ shift significantly more than those of cells far from it, and, on average, display a shift away from the LPZ.

Third, receptive field size increases at the early stages of functional recovery and decreases at the latest stages. Receptive fields remain larger than at baseline for cells close to the LPZ.

Fourth, orientation tuning is not differently affected in cells close and far from the LPZ. Despite a slightly higher instability of orientation selectivity of cells close to the LPZ, the analysis of tuning properties such as shift from preferred orientation, shift from preferred direction and bandwidth of all cells that were orientation selective at baseline showed only small, non-significant, differences after retinal lesions, both for cells close and far from the LPZ.

Recently, Abe et al. [1] used chronically implanted multi-electrode arrays in a longitudinal study of functional recovery after retinal lesions in monkey visual cortex. While the use of such arrays might lower the risk of a sampling bias towards a neuron subpopulation with receptive fields outside the lesioned area (Smirnakis et al. [71]), extracellular electrophysiological recordings are restricted to cells which show at least some activity, and even active units cannot be unmistakably assigned to the same cells over time. In contrast, two-photon calcium imaging is advantageous since it allows for the recording of neurons' responses regardless of their activity state, and cells can be reliably re-identified based on their morphology in subsequent sessions. Moreover, the recent development of the more sensitive genetically-encoded calcium indicator GCaMP6s (Chen et al. [14]) coupled with a structural marker (mRuby2, design by Tobias Rose), permitted the detection of smaller calcium transients, limited the acquisition of deleterious nuclear fluorescence and aberrant response effects characteristic of older GCaMP versions (Tian et al. [77], Zariwala et al. [84]) and made cell detection independent of activity state.

4.1 Visually-driven activity decreases close to the LPZ

In the early electrophysiological studies on the effects of retinal lesions by Eysel et al. [23], Kaas et al. [45], Gilbert and Wiesel [30] there were no quantifiable reports on activity levels after retinal lesions, either spontaneous or visually-driven. Horton and Hocking [38], using a very different approach to map activity, found with a cytochrome oxidase staining method in monkeys that a “hole” in cytochrome oxidase activity remains in the cortex even months after the retinal lesion, pointing to a profound depression of neuronal activity. In cats, in contrast, Giannikopoulos and Eysel [24] reported an early hyperactivity wave within the LPZ that subsided over time with the progression of functional recovery. Recently, Abe et al. [1] showed that, within the first week after binocular retinal lesions in monkeys, there was a transient recovery of visual responses in the LPZ, followed by a few weeks of decreased activity and 60-90% of responsive units within 2-3 months.

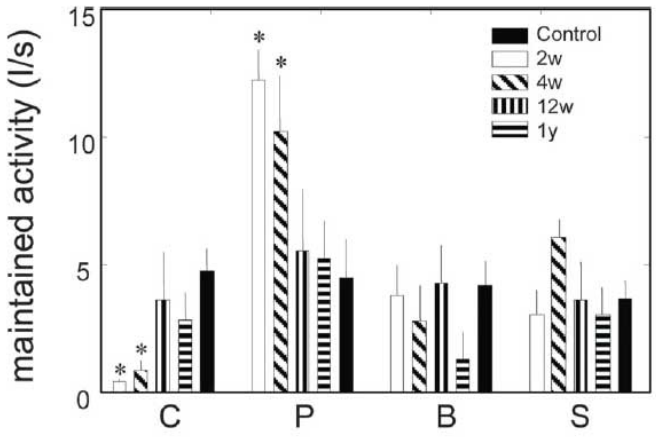

Figure 4.1.1 – Evoked activity levels at different time points after RL; from Giannikopoulos and Eysel [24]©. C: deafferented center; P: activity peak within LPZ; B: LPZ border; S: surround LPZ. Whereas at the center of the LPZ the activity levels drop significantly and are not recovered even a year after retinal lesions, within the LPZ the activity peak is significantly increased during the first month after the retinal lesion and then activity levels revert close to control levels. At the border region, activity levels even drop in comparison to controls at all time points but especially after one year. In the surround of the LPZ, there is only a certain increase in activity levels a month after retinal lesions, but overall activity levels remain around control levels at all time points.

To explore the effect of small retinal lesions on visually-driven activity in mice, I analyzed the responses to visual stimulation of neurons located close to the LPZ and, after retinal lesions, found a significant decrease of visually-driven activity that did not recover even two months after the loss of sensory input. Although this finding is in apparent contra-

diction to the results reported by Giannikopoulos and Eysel [24] and Abe et al. [1], in the present study I focused on regions in the periphery of the LPZ. Importantly, this finding is more in line with data from Horton and Hocking [38] and with Giannikopoulos and Eysel [24]'s report of decreased evoked activity in border regions than with their finding of increased activity after two weeks in peripheral regions. The former point could be explained either by the large difference in brain size between the two species (cats versus mice), or by a conceptual difference in the definition of border and surround regions.

Homeostatic plasticity has been found to play a role in the restoration of activity levels after complete retinal lesions in mice (Keck et al. [46]). After a short period of decreased activity, synaptic scaling occurs following the same time course as the increase in cortical activity levels, pointing to an homeostatic response to the previously decreased activity. Likewise, after monocular deprivation (MD) Lambo and Turrigiano [53] observed that synaptic and intrinsic homeostatic mechanisms jointly increase the excitability of L2/3 pyramidal neurons after prolonged MD, suggesting that homeostatic mechanisms contribute to the delayed gain of visual responsiveness during OD plasticity. However, in these studies homeostatic changes took place over time periods ranging from 24-48 hours, in the case of full retinal lesions, and up to 6 days in the MD study. In my data, as well as in Keck et al. [47] even after two months no full recovery of visually-driven activity could be detected, which would imply that if such homeostatic mechanisms were acting in this model, either they are of a really small scale and therefore cannot help drive the cells back to their initial response levels, or they take place at time points even after the time span of this study.

The work of Keck et al. [47, 48] on structural plasticity after retinal lesions showed not only that turnover rates for excitatory dendritic spines is lower in border regions than in the LPZ center but also that inhibitory spine and bouton densities were higher in these regions than in the center, pointing towards a plasticity gradient depending inversely on distance from the LPZ center. Based on this structural data, it is possible that since I analyzed cells located close but not within the LPZ, the plasticity and/or homeostatic changes driving

the functional recovery are not as strong as inside and therefore functional recovery only partial.

In agreement with the general decrease in visually-driven activity found for cells close to the LPZ, the peak amplitude at the preferred orientation was also significantly smaller for cells near the LPZ for a month after the lesion. This tendency towards normalization could reflect a change in the balance of excitation-inhibition possibly correlated to the structural changes found both for excitatory and inhibitory spines in regions surrounding the LPZ (Keck et al. [47, 48]). The lower excitatory spine dynamics and higher inhibitory spine density found for regions neighboring the LPZ when compared to those inside could explain the latency for the recovery of close to baseline peak amplitudes at the preferred orientation. On the other hand, it is possible that some of the aforementioned homeostatic mechanisms contribute to this effect.

In line with the reduced activity levels, after retinal lesions I observed a larger and significant reduction in receptive field detection rate for cells located close to the LPZ, with only about 40% of the receptive fields detected at baseline whereas for cells far from the LPZ about 60% could still be detected.

4.2 Neurons close to the LPZ show stronger shifts in receptive field position

A well known effect of retinal lesions is that they cause shifts in the receptive fields of neurons in the LPZ. Already in the first reports by Gilbert et al. [26], Kaas et al. [45], Gilbert [25], Gilbert and Wiesel [30] receptive fields of cells located within the LPZ were found to shift their positions towards the outside of the deprived region. In a process known as “filling-in” (Gilbert [25], Gilbert and Wiesel [30]), initially silent cells inside the LPZ regain activity soon followed by more and more cells that acquire new receptive fields just outside of the lesion. This finding was later confirmed by single-cell recordings in cats and monkeys (Giannikopoulos and Eysel [24], Abe et al. [1]). In mice, the only

functional study to date by Keck et al. [47] found an almost full recovery of visual function and complete filling-in of the LPZ, but it was not technically possible to determine the extent of the shift of individual cells affected by retinal lesion.

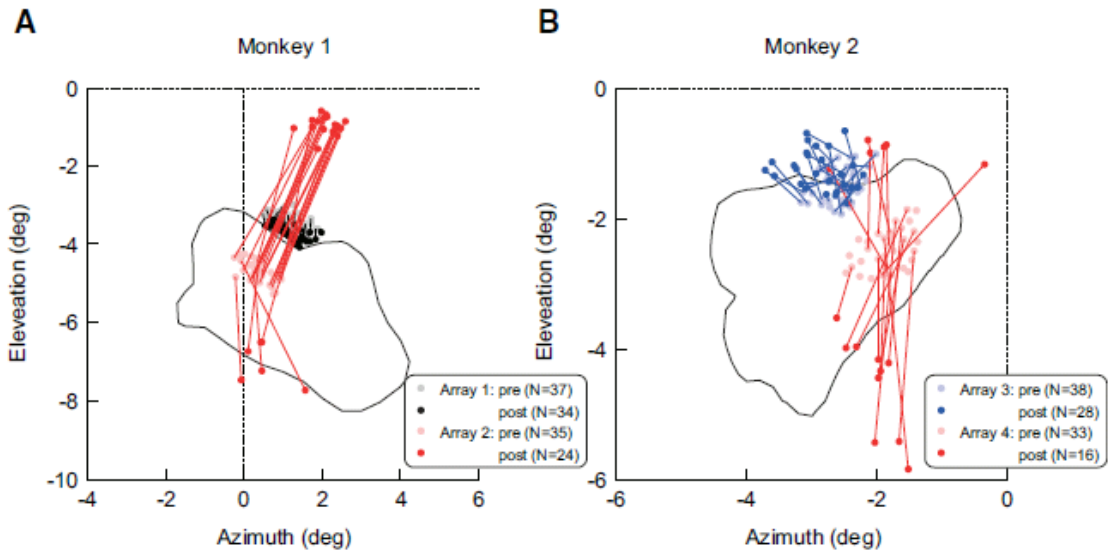

Figure 4.2.1 – Receptive field shifts in two monkeys after retinal lesions; from Abe et al. [1]. Pale and dark colored dots indicate pre- and post- lesion positions in both example monkeys, lines connecting the RF locations of the same electrodes and each color corresponding to a different array. Black lines: outline of the LPZ determined as the area where animals failed to make a saccade to a small target in $\geq$50% trials in a behavioral test. For receptive fields initially located within the LPZ the magnitude of the shift is larger than for those located at the border, but in all cases the direction of the shift points away from the LPZ. The small shift toward the LPZ displayed by the positions depicted in black might be due to retina contraction. Printed with permission.

To address the question of the effect of retinal lesions on receptive field positions in mice at the single cell level, I tracked receptive field position for neurons located both far and close to the LPZ for two months after retinal lesions. Overall, I found that for all cells located in regions close to the LPZ, the average shift of their receptive field centers with respect to their positions prior to retinal lesions was significantly larger at all time bins considered (early, intermediate and late), than the shift measured for receptive field centers of cells located far from the LPZ, which remained close to their initial positions. This result is in agreement with data from other animal models and methodologies (Gilbert et al. [26], Kaas et al. [45], Gilbert [25], Gilbert and Wiesel [30], Giannikopoulos and Eysel [24], Abe et al. [1]), suggesting that in mice shifts of receptive field positions is also a

hallmark of plasticity after retinal lesions.

In monkeys, receptive field shifts for cells within the LPZ have been measured to be between 3°-5° (Gilbert and Wiesel [30], Abe et al. [1]), whereas here I find that the average shift is far larger, around 16°, a result that is likely due to the massive differences in magnification factors between mice and monkeys, (as explained in section 1.2.1), which could also explain the more extensive "filling-in" observed in mice. Not only is the deprived cortical region of a much smaller size (a few hundred micrometers) compared to that of monkeys and cats (several millimeters), but also the size of the elements of the visual system does not scale with the massive differences in magnification factor between these species, as was previously mentioned. However, it is important to notice that I measured the receptive field shifts of cells located just outside the LPZ, and even if located in close proximity to it, there still might be differences to those within the LPZ. Abe et al. [1] found receptive field shifts for units located at the LPZ boundary to be smaller on average (0.52±0.04°) than those inside the LPZ (see figure 4.2.1 panel B), therefore it is possible that the RF shifts for neurons inside the LPZ in mice might be even larger than those of our population of cells close to the LPZ.

Similar to earlier reports (Gilbert et al. [26], Kaas et al. [45], Gilbert [25], Gilbert and Wiesel [30], Giannikopoulos and Eysel [24], Abe et al. [1]), when I performed a vector analysis to determine the mean direction of the shift of receptive field centers for cells close to the LPZ, I found that, in general, receptive fields tend to shift away from the LPZ border.

Despite the scarcity of previous data on the direction or size of the shift of receptive fields for cells located at neighboring regions of the LPZ, it is remarkable to find similar plasticity changes to those reported for cells inside the LPZ, which points to a recovery mechanism that extends beyond the LPZ boundary and that might have decreasing effects depending on distance from the LPZ center. This idea is supported both by structural (Keck et al. [47, 48]) and functional data (Giannikopoulos and Eysel [24]) with findings that correlate differential effects on LPZ center distance such as the different excitatory spine turnover

rates, inhibitory spine and bouton densities or visual activity levels in cats.

4.3 Receptive field size changes over time

Another property that has been found to be altered after retinal lesions is receptive field size. Gilbert [25] was the first to show an early increase in receptive field size for cells in the LPZ, which, during recovery returned back close to baseline size. This finding has been later confirmed by others like Giannikopoulos and Eysel [24], Abe et al. [1].

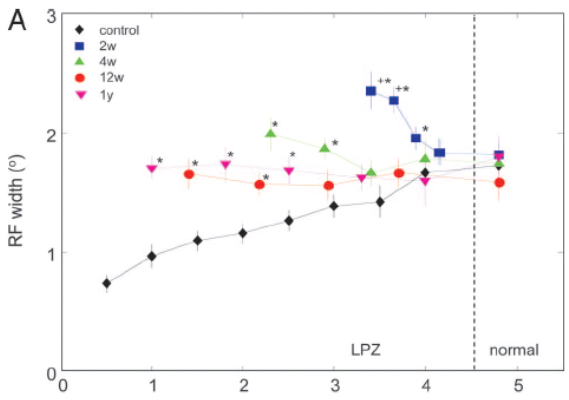

Figure 4.3.1 – RF width increases after retinal lesions and tends to normalize at longer recovery times in cats; from Giannikopoulos and Eysel [24]©. Dashed line represents the border of LPZ, each mark corresponds to a recording at different positions with respect to LPZ border. Black symbols represent control measurements in unlesioned animals.

To characterize changes to receptive field sizes after retinal lesions in mice, I measured receptive field area at baseline and found an average size of around 50 deg^2. Smith and Häusser [72] using two-photon calcium imaging in mice found mostly simple cells, with both ON and OFF subfields, and reported an average size for subfields of around 200 deg^2, much larger than the average size for receptive fields determined in this study. While this is a very similar study in the approach to receptive field mapping, there are several methodological differences that could account for the disparate results. First, the visual stimulation paradigms differed strongly: instead of a sparse-noise stimulus as in Smith and Häusser [72], I used local patch stimuli. Also stimulus size and stimulation time differed. Second, the calcium indicator was different. Smith and Häusser [72] employed a synthetic one, OGB1-AM, which allowed spike inference, which is so far not possible for GCaMP6s. Moreover, differences in receptive field size could be a direct consequence of the indicator employed in this study, since the known non-linearities of the fluorescence response

of GCaMP6s to increasing action potential numbers and its slow dynamics make a fine determination of receptive field size challenging (Chen et al. [14]). However, since the focus of this study was not to determine absolute receptive field sizes but rather characterizing relative changes of this parameter after retinal lesions, the receptive field sizes provided by this indicator do not necessarily challenge these results.

Similarly to what was described in the work by Gilbert [25], Giannikopoulos and Eysel [24], Abe et al. [1], I found that RF sizes of cells located close to the LPZ experienced a marked increase with respect to baseline early after retinal lesions. Receptive field sizes decreased slightly over time, but remained enlarged even two months after deprivation. In their study, Giannikopoulos and Eysel [24] found that receptive field size returned back to normal after three months; here I observed a tendency towards normalization of receptive field size that points in the direction of their results. Conversely, receptive fields of cells far from the LPZ also increased their size slightly at early time points after the retinal lesion, but over time they contracted back to their initial size, which is also in line with earlier data by Gilbert [25], Giannikopoulos and Eysel [24], Abe et al. [1].

4.4 Orientation tuning after retinal lesions

A key feature of neurons in V1 is orientation selectivity. Despite its importance, to date not much is known about the effects of retinal lesions on this property. Only Giannikopoulos and Eysel [24] and lately Abe et al. [1] have paid attention to this characteristic. Single-unit recordings in cats showed a maintained increase in tuning width for cells located inside the LPZ, which did not return to baseline levels even a year after sensory deprivation (Giannikopoulos and Eysel [24]). Conversely, Abe et al. [1] using microelectrode arrays in monkeys did not find a significant change in tuning width post-lesion nor did they find any changes to preferred orientation. To determine the sort of plasticity changes affecting orientation tuning in mice after small retinal lesions, I examined the potential differences in

tuning properties caused by retinal lesions between the two spatially defined cell groups, close and far to the LPZ.

Despite the fact that I found that, on average, cells close to the LPZ have a less stable orientation selectivity after retinal lesions, the average OSI for both regions remained similar after retinal lesions. Moreover, no significant differences could be detected between neurons located far or close to the LPZ in the range of the shift from preferred direction/preferred orientation or in bandwidth after retinal lesions.

This small variability in the tuning properties of neurons located close to the LPZ might be due to the particular organization of mouse V1 and the nature of the inputs driving the functional recovery.

The excitatory input provided by lateral cortico-cortical horizontal connections is thought to be crucial for the recovery of activity after retinal lesions (Darian-Smith and Gilbert [16], Das and Gilbert [18], Palagina et al. [65]). In animals with a cortical columnar organization such as cats or monkeys (Hubel and Wiesel [40], Hubel et al. [41]), the local horizontal connections within L2/3, which have been proven fundamental in the functional recovery after retinal lesions (Darian-Smith and Gilbert [17], Das and Gilbert [18], Palagina et al. [65]), link functionally similar columns (Malach et al. [57], Stettler et al. [73]). However, the functional interactions among columns are not restricted to those orientation-specific determined by the monosynaptic distribution of horizontal connections (Huang et al. [39]).

In contrast, in mouse V1 there is no functional architecture for orientation preference (see section 1.1), cells with different preferred orientations are arranged in what is termed a “salt-and-pepper” organization (Dräger and Olsen [22], Ohki et al. [63]), where neurons preferring different orientations are mixed together in a locally disorganized fashion. In addition, in the mouse visual cortex neurons connect preferentially to other neurons sharing their preferred orientation (Hofer et al. [35], Ko et al. [52, 51]). Furthermore, it was recently shown that V1 neurons receive the majority of their local excitation from a small number of strong inputs. These inputs are provided by only a few neurons with similar responses to visual features, thus mediating stimulus-specific response amplification in

cortical microcircuits. Furthermore, the neurons more strongly connected are those with similar receptive field structures (Cossell et al. [15]).

Based on this evidence, the relatively low variability in the tuning responses of cells close to the LPZ could be due, partly, to the salt-and-pepper organization of V1 which would prevent the loss of all lateral input encoding a certain orientation preference. Moreover, even when a number of connections are lost, just a few of those strong inputs remaining intact would be sufficient to maintain overall orientation tuning, and a certain jitter provided by strengthening of previously weaker inputs.

One remarkable feature of the functional reorganization after retinal lesions in mouse V1 is that even with receptive field size and position changing, tuning seem to remain quite stable. Considering the aforementioned evidence for strong and more relevant inputs coming from cells with similar receptive field structures, such a marked shift in receptive field position might be counterintuitive. However, the increase in receptive field width could be a response to the summation of the individual receptive fields of the strong inputs driving the recovery, and its shift the result of the average position of overlap of the receptive fields of those cells with higher response correlations to the deprived ones.

4.5 Synopsis: functional plasticity in the visual cortex after retinal lesions

In summary, I demonstrated that after partial retinal lesions in mice, the receptive fields of neurons located close to the LPZ experience a significant shift from their baseline positions and away from the LPZ, while receptive field size increases at the early stages and tends to return back to baseline at later time points. These findings are in agreement with previous reports from various animal models, even though this study did not focus on neurons within the LPZ but on its neighboring regions, which points towards a general model of functional plasticity of decreasing magnitude dependent on distance from the LPZ center.

Furthermore, I could prove that general visually-driven activity levels are significantly reduced after retinal lesions in regions close to the LPZ, and that this decrease in activity levels is maintained over two months after sensory deprivation. This finding could be the result of a slower time course in the recovery of regions outside the LPZ, given the lower structural plasticity rates found in these areas (Keck et al. [47, 48]). Longer recovery times might lead back to baseline activity levels, a possibility favored by the finding that even when peak amplitude is significantly decreased in these regions right after retinal lesions, there is a tendency towards normalization at later time points. In order to clarify this issue it would be necessary to follow up the functional recovery after retinal lesions for longer periods than two months.

Finally, I found that even when the orientation selectivity of neurons near the LPZ appears less stable than for those far from it, in general, orientation tuning does not change significantly after retinal lesions, neither for cells close nor far from the LPZ. This resilience of orientation tuning points to network effects, which would compensate the loss of sensory input, thus maintaining the overall response properties at the population level.

Bibliography

[1] Abe, H., J. N. J. McManus, N. Ramalingam, W. Li, S. a. Marik, S. Meyer zum Alten Borgloh, and C. Gilbert: 2015, 'Adult cortical plasticity studied with chronically implanted electrode arrays'. *J Neurosci.* **35**(6), 2778–2790.

[2] Albus, K. and F. Donate-Oliver: 1977, 'Cells of origin of occipito-pontine projection in cat -functional properties and intracortical location'. *Exp. Brain. Res.* **28**, 167–174.

[3] Baker, C., D. Dilks, E. Peli, and N. Kanwisher: 2008, 'Reorganization of visual processing in macular degeneration: replication and clues about the role of foveal loss'. *Vision Res.* **48**, 1910–1919.

[4] Baker, C., E. Peli, N. Knouf, and N. Kanwisher: 2005, 'Reorganization of visual processing in macular degeneration'. *J Neurosci.* **25**, 614–618.

[5] Baseler, H., A. Gouws, K. Haak, C. Racey, M. Crossland, A. Tufail, G. Rubin, F. Cornelissen, and A. Morland: 2011, 'Large-scale remapping of visual cortex is absent in adult humans with macular degeneration'. *Nat Neurosci.* **14**(5), 649–55.

[6] Bayer, M.: 2013, 'Through the eyes of a mouse'. *Nat News* **502**, 156–158.

[7] Berens, P.: 2009, 'Circstat:A MATLAB toolbox for circular statistics'. *J Stat Software.* **31**(10).

[8] Berridge, M., P. Lipp, and M. Bootman: 2000, 'The versatility and universality of calcium signalling'. *Nat. Rev. Mol. Cell. Biol.* **1**, 11–21.

[9] Bonhoeffer, T. and A. Grinvald: 1991, 'Iso-orientation domains in cat visual-cortex are arranged in pinwheel-like patterns'. *Nature* **353**, 429–431.

[10] Bonin, V., M. Histed, S. Yurgenson, and R. Reid: 2011, 'Local diversity and fine-scale organization of receptive fields in mouse visual cortex'. *J. Neurosci.* **31**(50), 18506–18521.

[11] Botelho, E., C. Ceriatte, J. Soares, R. Gattass, and M. Fiorani: 2014, 'Quantification of early stages of cortical reorganization of the topographic map of V1 following retinal lesions in monkeys'. *Cereb. Cortex* **24**(1), 1–16.

[12] Calford, B., Y. Chino, U. Das, A.and Eysel, C. Gilbert, S. Heinen, J. Kaas, and S. Ullman: 2005, 'Neuroscience: rewiring the adult brain'. *Nature* **438**(7065), discussion E3–4.

[13] Calford, B., C. Wang, V. Taglianetti, W. Waleszczyk, W. Burke, and B. Dreher: 2000, 'Plasticity in adult cat visual cortex (area 17) following circumscribed monocular lesions of all retinal layers'. *J Physiol.* **524**, 587–602.

[14] Chen, T., T. Wardill, Y. Sun, S. Pulver, S. Renninger, A. Baohan, E. Schreiter, R. Kerr, M. B. Orger, V. Jayaraman, L. L. Looger, K. Svoboda, and D. Kim: 2013, 'Ultrasensitive fluorescent proteins for imaging neuronal activity'. *Nature* **499**(7458), 295–300.

[15] Cossell, L., M. Iacaruso, D. Muir, R. Houlton, E. Sader, H. Ko, S. Hofer, and M.-F. T.D.: 2015, 'Functional organization of excitatory synaptic strength in primary visual cortex'. *Nature* **518**(7539), 399–403.

[16] Darian-Smith, C. and C. Gilbert: 1994, 'Axonal sprouting accompanies functional reorganization in adult cat striate cortex'. *Nature* **368**, 737–40.

[17] Darian-Smith, C. and C. Gilbert: 1995, 'Topographic and monkey reorganization in the striate cortex of the adult Is cortically mediated'. *J Neurosci.* **15**(3), 1631–1647.

[18] Das, A. and C. Gilbert: 1995, 'Long-range horizontal connections and their role in cortical reorganization revealed by optical recording of cat primary visual cortex'. *Nature* **375**, 780–784.

[19] Denk, W., J. Strickler, and W. Webb: 1990, '2-photon laser scanning fluorescence microscopy'. *Science* **248**, 73–76.

[20] Douglas, R. and K. Martin: 2004, 'Neuronal circuits of the neocortex'. *Annu. Rev. Neurosci.* **27**, 419–451.

[21] Dräger, U.: 1975, 'Receptive-fields of single cells and topography in mouse visual-cortex'. *J Comp Neurol.* **160**, 269–289.

[22] Dräger, U. and J. Olsen: 1980, 'Origins of crossed and uncrossed retinal projections in pigmented and albino mice'. *J Comp. Neurol.* **191**(2), 383–412.

[23] Eysel, U., F. Gonzalez-Aguilar, and U. Mayer: 1980, 'A functional sign of reorganization in the visual system of adult cats: lateral geniculate neurons with displaced receptive fields after the lesion of the nasal retina'. *Brain Research* **181**, 285–300.

[24] Giannikopoulos, D. and U. Eysel: 2006, 'Dynamics and specificity of cortical map reorganization after retinal lesions'. *Proc Natl Acad Sci U S A* **103**(28), 10805–10.

[25] Gilbert, C.: 1992, 'Horizontal integration and cortical dynamics'. *Neuron* **9**(1), 1–13.

[26] Gilbert, C., J. Hirsch, and T. Wiesel: 1990, 'Lateral interactions in visual cortex'. *Cold Spring Harb. Symp. Quant. Biol.* **55**, 663–677.

[27] Gilbert, C. and J. Kelly: 1975, 'Projections of cells in different layers of cats visual-cortex'. *Nat Neurol.* **163**, 81–105.

[28] Gilbert, C. and T. Wiesel: 1979, 'Morphology and intra-cortical projections of functionally characterized neurons in the cat visual-cortex'. *Nature* **280**, 120–125.

[29] Gilbert, C. and T. Wiesel: 1983, 'Functional organization of the visual cortex'. *Prog Brain Res* **58**, 209–18.

[30] Gilbert, C. and T. Wiesel: 1992, 'Receptive field dynamics in adult primary visual cortex'. *Nature* **356**(6365), 150–152.

[31] Grewe, B., D. Langer, H. Kasper, B. Kampa, and F. Helmchen: 2010, 'High-speed in vivo calcium imaging reveals neuronal network activity with near-millisecond precision'. *Nat Methods.* **7**, 399–391.

[32] Grienberger, C. and A. Konnerth: 2012, 'Imaging calcium in neurons'. *Neuron* **73**(5), 862–85.

[33] Helmchen, F. and W. Denk: 2005, 'Deep tissue two-photon microscopy'. *Nat Methods.* **2**(12), 932–40.

[34] Hendel, T., M. Mank, B. Schnell, O. Griesbeck, A. Borst, and D. Reiff: 2008, 'Fluorescence changes of genetic calcium indicators and OGB-1 correlated with neural activity and calcium'. *J Neurosci.* **28**(29), 7399 –7411.

[35] Hofer, S., H. Ko, B. Pichler, J. Vogelstein, H. Ros, H. Zeng, E. Lein, N. Lesica, and T. Mrsic-Flogel: 2011, 'Differential connectivity and response dynamics of excitatory and inhibitory neurons in visual cortex'. *Nat Neurosci.* **14**(8), 1045–52.

[36] Holtmaat, A., T. Bonhoeffer, D. Chow, J. Chuckowree, V. De Paola, S. Hofer, M. Hübener, T. Keck, G. Knott, W. Lee, R. Mostany, T. Mrsic-Flogel, E. Nedivi, C. Portera-Cailliau, K. Svoboda, J. Trachtenberg, and L. Wilbrecht: 2009, 'Long-term, high-resolution imaging in the mouse neocortex through a chronic cranial window'. *Nat Protoc.* **4**(8), 1128–44.

[37] Holtmaat, A., L. Wilbrecht, G. Knott, E. Welker, and K. Svoboda: 2006, 'Experience-dependent and cell-type-specific spine growth in the neocortex'. *Nature* **441**, 979–983.

[38] Horton, J. and D. Hocking: 1998, 'Monocular core zones and binocular border strips in primate striate cortex revealed by the contrasting effects of enucleation, eyelid suture, and retinal laser lesions on cytochrome oxidase activity'. *J Neurosci.* **18**(14), 5433–5455.

[39] Huang, X., Y. Elyada, W. Bosking, T. Walker, and D. Fitzpatrick: 2014, 'Optogenetic assessment of horizontal interactions in primary visual cortex'. *J Neurosci.* **34**(14), 4976–4990.

[40] Hubel, D. and T. Wiesel: 1962, 'Receptive fields, binocular interaction and functional architecture in cats visual cortex'. *J Physiol.* **162**, 106–154.

[41] Hubel, D., T. Wiesel, and M. Stryker: 1977, 'Orientation columns in macaque monkey visual cortex demonstrated by the 2-deoxyglucose autoradiographic technique'. *Nature* **269**(5626), 328–30.

[42] Hübener, M.: 2003, 'Mouse visual cortex'. *Curr Opin Neurobiol.* **13**(4), 413–420.

[43] Hübener, M. and T. Bonhoeffer: 2014, 'Neuronal plasticity: beyond the critical period'. *Cell* **159**(4), 727–737.

[44] Hübener, M. and J. Bolz: 1988, 'Morphology of identified projection neurons in layer-5 of rat visual-cortex'. *Neurosci Lett.* **94**, 76–81.

[45] Kaas, J., L. Krubitzer, Y. Chino, A. Langston, E. Polley, and N. Blair: 1990, 'Reorganization of retinotopic cortical maps in adult mammals after lesions of the retina'. *Science* **248**, 229–231.

[46] Keck, T., G. Keller, R. Jacobsen, U. Eysel, T. Bonhoeffer, and M. Hübener: 2013, 'Synaptic scaling and homeostatic plasticity in the mouse visual cortex in vivo'. *Neuron* **80**(2), 327–34.

[47] Keck, T., T. Mrsic-Flogel, M. Vaz Afonso, U. Eysel, T. Bonhoeffer, and M. Hübener: 2008, 'Massive restructuring of neuronal circuits during functional reorganization of adult visual cortex'. *Nat Neurosci* **11**(10), 1162–7.

[48] Keck, T., V. Scheuss, R. Jacobsen, C. J. Wierenga, U. Eysel, T. Bonhoeffer, and M. Hübener: 2011, 'Loss of sensory input causes rapid structural changes of inhibitory neurons in adult mouse visual cortex'. *Neuron* **71**(5), 869–82.

[49] Kerlin, A., M. Andermann, V. Berezovskii, and R. Reid: 2010, 'Broadly tuned response properties of diverse inhibitory neuron subtypes in mouse visual cortex'. *Neuron* **67**(5), 858–71.

[50] Kerr, J. and W. Denk: 2008, 'Imaging in vivo: watching the brain in action'. *Nat Rev Neurosci.* **9**(3), 195–205.

[51] Ko, H., L. Cossell, C. Baragli, J. Antolik, C. Clopath, S. Hofer, and T. Mrsic-Flogel: 2013, 'The emergence of functional microcircuits in visual cortex'. *Nature* **496**(7443), 96–100.

[52] Ko, H., S. Hofer, B. Pichler, K. Buchanan, P. J. Sjöström, and T. Mrsic-Flogel: 2011, 'Functional specificity of local synaptic connections in neocortical networks'. *Nature* **473**(7345), 87–91.

[53] Lambo, M. and G. Turrigiano: 2013, 'Synaptic and intrinsic homeostatic mechanisms cooperate to increase L2/3 pyramidal neuron excitability during a late phase of critical period plasticity'. *J Neurosci.* **33**(20), 8810–9.

[54] Li, Y., S. Van Hooser, M. Mazurek, L. White, and D. Fitzpatrick: 2008, 'Experience with moving visual stimuli drives the early development of cortical direction selectivity'. *Nature* **456**(7224), 952–956.

[55] Liu, B., Y. Li, W. Ma, C. Pan, L. Zhang, and H. Tao: 2011, 'Broad inhibition sharpens orientation selectivity by expanding input dynamic range in mouse simple cells'. *Neuron* **71**(3), 542–54.

[56] Lund, J., R. Lund, A. Hendrickson, A. Bunt, and A. Fuchs: 1975, 'Origin of efferent pathways from primary visual-cortex, area 17, of macaque monkey as shown by retrograde transport of horseradish-peroxidase'. *J. Comp. Neurol.* **164**, 287–303.

[57] Malach, R., M. Amir, Y. andHarel, and A. Grinvald: 1993, 'Relationship between intrinsic connections and functional architecture revealed by optical imaging and in vivo targeted biocytin injections in primate striate cortex'. *Proc Natl Acad Sci U S A* **90**, 10469–10473.

[58] Mangini, N. and A. Pearlman: 1980, 'Laminar distribution of receptive field properties in the primary visual cortex of the mouse'. *J Comp Neurol.* **193**, 203–222.

[59] Marik, S. a., H. Yamahachi, S. Meyer zum Alten Borgloh, and C. D. Gilbert: 2014, 'Large-scale axonal reorganization of inhibitory neurons following retinal lesions'. *J Neurosci.* **34**(5), 1625–1632.

[60] Merzenich, M., R. Nelson, M. Stryker, M. Cynader, A. Schoppmann, and J. Zook: 1984, 'Somatosensory cortical map changes following digitamputation in adult monkeys'. *J Comp Neurol.* **224**, 591–605.

[61] Métin, C., P. Godement, and M. Imbert: 1988, 'The primary visual cortex in the mouse: receptive field properties and functional organization'. *Exp Brain Res.* **69**(3), 594–612.

[62] Niell, C. and M. Stryker: 2008, 'Highly selective receptive fields in mouse visual cortex'. *J Neurosci.* **28**(30), 7520–36.

[63] Ohki, K., C. S, Y. ChŽg, P. Kara, and R. Reid: 2005, 'Functional imaging with cellular resolution reveals precise micro-architecture in visual cortex'. *Nature* **433**, 597–603.

[64] Orbach, H., L. Cohen, and A. Grinvald: 1985, 'Optical mapping of electrical-activity in rat somatosensory and visual-cortex'. *J Neurosci.* **5**, 1886–1895.

[65] Palagina, G., U. Eysel, and D. Jancke: 2009, 'Strengthening of lateral activation in adult rat visual cortex after retinal lesions captured with voltage-sensitive dye imaging in vivo'. *Proc Natl Acad Sci U S A* **106**(21), 8743–7.

[66] Recanzone, G., C. Schreiner, and M. Merzenich: 1993, 'Plasticity in the frequency representation of primary auditory cortex following discrimination training in adult owl monkeys'. *J Neurosci.* **13**, 87–103.

[67] Ringach, D., R. Shapley, and M. Hawken: 2002, 'Orientation selectivity in macaque V1: diversity and laminar dependence'. *J Neurosci.* **22**(13), 5639–5651.

[68] Robertson, D. and D. Irvine: 1989, 'Plasticity of frequency organization in auditory cortex of guinea pigs with partial unilateral deafness'. *Journal Comp Neurol* **282**, 456–71.

[69] Runyan, C., J. Schummers, A. Van Wart, S. Kuhlman, N. Wilson, Z. J. Huang, and M. Sur: 2010, 'Response features of parvalbumin-expressing interneurons suggest precise roles for subtypes of inhibition in visual cortex'. *Neuron* **67**(5), 847–857.

[70] Schuett, S., T. Bonhoeffer, and M. Hübener: 2002, 'Mapping retinotopic structure in mouse visual cortex with optical imaging'. *J Neurosci.* **22**(15), 6549–59.

[71] Smirnakis, S., A. Brewer, M. Schmid, A. Tolias, A. Schüz, M. Augath, W. Inhoffen, B. Wandell, and N. Logothetis: 2005, 'Lack of long-term cortical reorganization after macaque retinal lesions'. *Nature* **435**(7040), 300–7.

[72] Smith, S. and M. Häusser: 2010, 'Parallel processing of visual space by neighboring neurons in mouse visual cortex'. *Nat Neurosci* **13**(9), 1144–1149.

[73] Stettler, D., A. Das, J. Bennett, and C. Gilbert: 2002, 'Lateral connectivity and contextual interactions in macaque primary visual cortex'. *Neuron* **36**, 739–750.

[74] Stettler, D., H. Yamahachi, W. Li, W. Denk, and C. Gilbert: 2006, 'Axons and synaptic boutons are highly dynamic in adult visual cortex'. *Neuron* **49**, 877–887.

[75] Stosiek, C., O. Garaschuk, K. Holthoff, and A. Konnerth: 2003, 'In vivo two-photon calcium imaging of neuronal networks'. *Proc* **100**(12), 7319–24.

[76] Tian, L., S. Hires, and L. Looger: 2012, 'Imaging neuronal activity with genetically encoded calcium indicators'. *Cold Spring Harb Protoc.* **2012**(6), 647–56.

[77] Tian, L., S. Hires, T. Mao, D. Huber, M. Chiappe, S. Chalasani, L. Petreanu, J. Akerboom, S. a. McKinney, E. Schreiter, C. Bargmann, V. Jayaraman, K. Svoboda, and L. Looger: 2009, 'Imaging neural activity in worms, flies and mice with improved GCaMP calcium indicators'. *Nat* **6**(12), 875–81.

[78] Trachtenberg, J., B. Chen, G. Knott, J. Feng, G.P. andSanes, E. Welker, and K. Svoboda: 2002, 'Long-term in vivo imaging of experience-dependent synaptic plasticity in adult cortex'. *Nature* **420**, 788–794.

[79] Tsien, R. and R. Tsien: 1990, 'Calcium channels stores and oscillations'. *Annu Rev Cell Biol* **6**, 715–760.

[80] Valverde, F.: 1968, 'Structural changes in the area striata of the mouse after enucleation'. *Exp Brain Res.* **5**(4), 274–92.

[81] Wang, Q. and A. Burkhalter: 2007, 'Area map of mouse visual cortex'. *J Comp Neurol.* **357**, 339 –357.

[82] Wilks, T., A. Harvey, and J. Rodger: 2013, *Functional Brain Mapping and the Endeavor to Understand the Working Brain*. InTech. Chapter 12: Seeing with two eyes: integration of binocular projections in the brain.

[83] Yamahachi, H., S. Marik, J. McManus, W. Denk, and C. Gilbert: 2009, 'Rapid axonal sprouting and pruning accompany functional reorganization in primary visual cortex'. *Neuron* **64**(5), 719–29.

[84] Zariwala, H. a., B. G. Borghuis, T. M. Hoogland, L. Madisen, L. Tian, C. I. De Zeeuw, H. Zeng, L. L. Looger, K. Svoboda, and T.-W. Chen: 2012, 'A Cre-Dependent GCaMP3 reporter mouse for neuronal imaging in vivo'. *J Neurosci.* **32**(9), 3131–3141.

Acknowledgments

First I would like to thank my supervisor Mark Hübener, for his constant support and his positive outlook over the whole of this “enterprise”. For being available for discussions and therefore helping expedite getting to the finish line. For understanding that there is more science than inside a microscope room and his understanding of the difficulties of a scientific career.

Next I have to thank the collaborators of this project, because without their help and support this thesis would not have been possible. Ulf Eysel, who came specially to Munich just to lesion our mice, Johannes Dahmen who provided some tips on stimulation and analysis code for receptive field mapping, Tobias Rose who designed the double construct used for 2p-imaging and above all, I want to thank Pieter Golstein for his technical support and his contribution to data analysis. There was a before and after in this project since his arrival to the team, and I am grateful for that. I also want to thank Tara Keck for her constant interest and support since the beginning of this project. Thanks to Frank Voss and Volker Staiger for technical support and Claudia Marget-Hahn for her help in all administrative matters and more.

For support, training, and funding, I thank the International Max Planck Research School for Life Sciences.

Acknowledgments

I want to say thank you to my colleagues, specially “my girls” for all the good times spent in and outside the lab, and our profound discussions on science and science politics.

I have to thank once again the support from my best friends and former colleagues, Rob Jelier and Irene González, who helped me both technically, with good and fruitful scientific discussions and valuable input, and emotionally over the course of this project.

All of my friends, far and close, Patri, Violeta, Andreia, Phil, Dani, Bárbara, Helen, Isina, Olivia, Ander and so many others have made everything easier with just a glass of wine and a good laugh. Thanks for that. And I could not forget about the unpredictable R. who shared with me the sun. Thank you for rescuing me from the cold.

Last, but not least, I want to thank my family for they are always there for me: no matter how far, no matter how tough or ugly things get, I know I can rely on them. It is because of them I got this far, and it is to them that I dedicate this thesis.